

**DESIGN AND FABRICATION OF A HYBRID NANOPARTICLE-WICK  
HEAT SINK STRUCTURE FOR THERMOELECTRIC GENERATORS IN  
LOW-GRADE HEAT UTILIZATION**

by

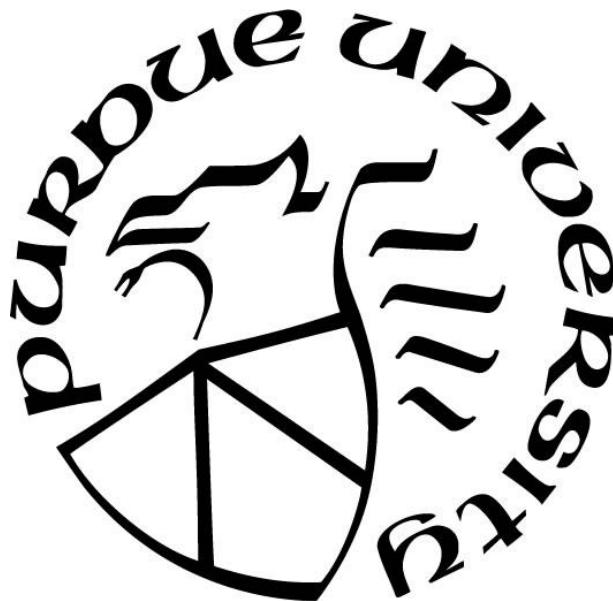
**Michael Daniel Akuma Ozeh**

**A Thesis**

*Submitted to the Faculty of Purdue University*

*In Partial Fulfillment of the Requirements for the degree of*

**Master of Science in Mechanical Engineering**



Department of Mechanical and Civil Engineering

Hammond, Indiana

December 2019

**THE PURDUE UNIVERSITY GRADUATE SCHOOL**  
**STATEMENT OF COMMITTEE APPROVAL**

**Dr. A. G. Agwu Nnanna, Chair**

Department of Mechanical and Civil Engineering

**Dr. Harvey Abramowitz, Co-Chair**

Department of Mechanical and Civil Engineering

**Dr. Chandramouli Viswanatha Chandramouli**

Department of Mechanical and Civil Engineering

**Dr. Nuri Zeytinoglu**

Department of Mechanical and Civil Engineering

**Approved by:**

Dr. Chenn Q. Zhou

## ACKNOWLEDGMENTS

I wish to express my deepest gratitude to a lot of people that contributed to the success of this academic program through their immense support and encouragement.

First and foremost, I would like to thank Professor Agbai George Agwu Nnanna for giving me the opportunity to pursue my Master's degree program under his tutelage at Purdue University and Purdue Water Institute respectively. I deeply appreciate his comprehensive guidance, incisive evaluation, encouragement and support throughout the process, and will always be grateful for his belief in me to accomplish the research objectives despite all the challenges encountered. I am equally grateful to Purdue Water Institute for financially supporting my research.

My deep appreciation also goes to Professor Harvey Abramowitz, Professor Chandramouli Viswanathan and Professor Nuri Zeytinoglu for serving as my committee members and lending their time, knowledge and expertise to my work; my colleagues Emekwo Ukoha, Uzumma Ozeh, Ashreet Mishra, David Okposio and Obinna Aronu, for their helpful contributions during the course of my research work.

I am deeply grateful to my parents -- Daniel Akuma Ozeh and Grace Akuma Ozeh -- and my siblings for their prayers, love and unwavering support; I will always be grateful to Dr. Lebe Nnanna, Joseph Ogba Ozeh, Oze Kalu Oze, Ada Eme Nwojo and Onuoha Ozeh for their support, guidance and prayers; my family and friends Samuel Ozeh, Williams Oged, Michael Okorie, Ikenna Ezwugwu and many others for their unreserved love, friendship and immeasurable support, which was critical to my success in this program.

I also greatly appreciate Ma Susan and Pa Dave, my parents-in-the-Lord who have been so supportive of my journey since we met in Life Point Church. You will always be family to me. In general, I am grateful to my local church (Life Point Church, Hammond Indiana) for their consistent love and support.

# TABLE OF CONTENTS

LIST OF TABLES .....	6
LIST OF FIGURES .....	7
LIST OF ABBREVIATIONS.....	9
GLOSSARY .....	10
ABSTRACT.....	12
CHAPTER 1. INTRODUCTION .....	13
1.1 Overview.....	13
1.2 Objectives and Scope.....	17
CHAPTER 2. LITERATURE REVIEW .....	18
2.1 Thermoelectric Materials.....	18
2.1.1 Organic Thermoelectric Materials.....	18
2.1.2 Inorganic Thermoelectric Materials .....	18
2.1.3 Metal Chalcogenides .....	19
2.1.4 Bismuth Telluride Thermoelectrics .....	19
2.1.5 Figure of Merit (zT).....	19
2.2 Thermoelectric Effects.....	22
2.3 Thermoelectric Generators.....	24
2.3.1 Advantages and Applications of Thermoelectric Generators .....	26
2.4 Cooling Techniques for Thermoelectric Generators.....	27
2.4.1 Active and Passive Heat Sinks .....	28
2.4.2 Passive Cooling Systems for TEGs .....	30
2.4.3 Evaporative Cooling using Heat Pipes and Nanofluids.....	31
CHAPTER 3. RESEARCH METHODOLOGY .....	35
3.1 Materials and Preliminary Tests .....	35
3.1.1 The Thermoelectric modules .....	35
3.1.2 The Wick .....	36
3.1.2.1 <i>Immobilization of nanoparticles on the wick</i> .....	36
3.1.2.2 <i>Porosity, Effective Conductivity and Capillarity of the wick</i> .....	38

3.1.3	Procedure for comparing the integrated wick with a plain PE wick and other conventional evaporative cooling apparatus .....	40
3.1.4	Procedure for tests on nanoparticle percent fraction for immobilization and the effect of wick thickness .....	43
3.2	Main Setup Process Flow Schematic and Design.....	45
3.3	Design Calculations .....	47
3.3.1	Heat Sink Pressure.....	47
3.3.2	Fluid Volume and Rate of Evaporation .....	47
3.3.3	Wick Boiling Limit.....	48
3.3.4	Pressure Drop and Permeability .....	49
3.3.5	Heat Transfer from the Heat Sink to the Ambient.....	50
CHAPTER 4.	RESULTS AND DISCUSSION .....	53
4.1	Linearity of Voltage Increment with Number of Modules .....	53
4.2	Seebeck Coefficient of the Modules .....	53
4.3	Effectiveness of the Integrated PE Wick Compared to a Heat Pipe and Metal Wick .....	56
4.4	Thermal Leakage to the Reservoir/Compensation Channels.....	59
4.5	Attrition of Immobilized Nanoparticles on the Wick .....	60
4.6	Nanoparticle Percent Fraction for Immobilization .....	62
4.7	Effect of Wick Thickness on the Integrated and Non-Integrated Wicks .....	65
4.8	Completed Heat Sink Test Run to Obtain 5V by Harvesting Low-Grade Heat .....	69
CHAPTER 5.	CONCLUSION AND RECOMMENDATIONS.....	72
REFERENCES	.....	74

## LIST OF TABLES

Table 1: Advantages of Thermoelectric Modules.....	26
Table 2: Properties of the Bi <sub>2</sub> Te <sub>3</sub> modules.....	35
Table 3: Wick properties.....	40
Table 4: Heat loads used in the experiment.....	43
Table 5: Power supplied to the heaters for the experiment.....	44
Table 6: Summary of heat transfer calculations on heat sink prototype.....	51
Table 7: Determination of immobilization wt/wt and attrition of immobilized nanoparticles.....	60
Table 8: Conductance results.....	63

## LIST OF FIGURES

Figure 1: A heat pipe's working principle .....	14
Figure 2: Loop Heat Pipe .....	15
Figure 3: Thermoelectric module .....	20
Figure 4: Figure of Merit (zT) as a function of temperature for several high-efficiency TEGs... ..	22
Figure 5: Seebeck and Peltier effects .....	23
Figure 6: Schematic of a TEG .....	25
Figure 7: Effect of increasing cold side temperature on thermoelectric efficiency for a hypothetical hot side temperature of 1030°C .....	28
Figure 8: Classification of TEG cooling technologies.....	29
Figure 9: The Bi <sub>2</sub> Te <sub>3</sub> TEC1-12706 thermoelectric modules.....	35
Figure 10: The PE wick .....	36
Figure 11: SEM image of plain PE wick before immobilization and a 20-micron view of the wick under a microscope after immobilization.. ..	37
Figure 12: Setup for finding the effective conductivity of the wick.....	38
Figure 13: To determine the rise (m/s), hence capillarity (mm/hr) of water along the wick.....	39
Figure 14: Picture of the setup with heat pipes.....	41
Figure 15: Picture and schematic of the setup with metal wick.. ..	41
Figure 16: Setup schematic of tests with the PE wick.....	42
Figure 17: Setup for nanoparticle percent fraction and thickness tests. . ..	44
Figure 18: Process flow schematic .....	45
Figure 19: Heat sink design .....	46
Figure 20: Wick support, top view.. ..	46
Figure 21: Dominating flow pattern from compensation channel across the wick. ....	48
Figure 22: Calculated boiling limit comparisons.....	49
Figure 23: Heat sink geometry schematic.....	50
Figure 24: Change in voltage with increase in the number of thermoelectric modules. ....	53
Figure 25: First experiment on increase in voltage with change in $\Delta T$ .....	54
Figure 26: Second experiment on increase in voltage with change in $\Delta T$ .....	54
Figure 27: The TEG evaporator area.. ..	55

Figure 28: Variation of heat source and heat sink temperature with time. ....	56
Figure 29: Voltage comparison for the different experiments.....	58
Figure 30: Temporal evolution of temperature in reservoir/compensation channels .....	59
Figure 31: Relationship between the vol/vol % of alumina suspension in working fluid and the final wt/wt % of Alumina immobilization on the PE wick.....	60
Figure 32: Bar chart showing negligible erosion of immobilized nanoparticles ( $\pm 1\%$ ).....	61
Figure 33: Conductance of the wick under different nanoparticle immobilization percentages ..	62
Figure 34: Comparison of the conductance of the wicks with the base case ( $\pm 8\%$ ) .....	63
Figure 35: Temperature difference and voltage results for 0.024” wick .....	65
Figure 36: Temperature difference and voltage results for 0.062” wick .....	66
Figure 37: Temperature difference and voltage results for 0.125” wick .....	67
Figure 38: Temperature difference and voltage results for 0.250” wick .....	67
Figure 39: Summary of voltage results for all the wicks .....	68
Figure 40: Temporal evolution of heat sink and source temperature, and voltage (0 m/s). ....	69
Figure 41: Temporal evolution of heat sink and source temperature, and voltage (< 2 m/s). ....	70
Figure 42: Integrated PE wick heat sink outperformed an active heat sink from a recent study..	71

## LIST OF ABBREVIATIONS

Al <sub>2</sub> O <sub>3</sub>	Aluminum Oxide
Alumina	Aluminum Oxide
Bi <sub>2</sub> Te <sub>3</sub>	Bismuth Telluride
COP	Coefficient of Performance
Cu	Copper
DC	Direct Current
DI	De-Ionized
DMAc	N-N-Dimethylacetamide
GPa	Gigapascal
H <sub>2</sub> O	Water
HOMO	Highest Occupied Molecular Orbital
LUMO	Lowest Unoccupied Molecular Orbital
MTBF	Mean Time Before Failure
Nu	Nusselt's number
PE	Polyethylene
Pr	Prandtl's number
Re	Reynold's number
RTG	Radioisotope Thermoelectric Generator
TE	Thermoelectric
TEG/TEGs	Thermoelectric Generator/Thermoelectric Generators
vol./vol.	Volume ratio
wt./wt.	Weight ratio
zT	Thermoelectric Figure of Merit

## GLOSSARY

$A_p/A_n$	Area of the positive and negative TE elements
$\alpha$	Seebeck Coefficient
$\alpha_p/\alpha_n$	Seebeck Coefficient of the positive/negative TE elements
$D_p/D_n$	Diameter of the positive and negative TE elements
$\Delta/\Delta T$	Difference/Temperature difference
$E_g$	Band-gap (eV)
$\eta_{th}$	Thermal efficiency
$h$	Heat transfer coefficient
$I$	Current
$k$	Thermal conductivity
$K$	Kelvins
$L_p/L_n$	Length of the positive and negative TE elements
$\lambda_w$	Effective conductivity of the wick
m (time)	Minutes
n-type	Semiconductor with electrons as majority charge carriers (net negative)
$P$	Power output
$P_J$	Joule's effect power contribution
$P_F$	Fourier's effect power contribution
$P_T$	Thompson's effect power contribution
$\pi$	Peltier Coefficient (V)
p-type	Semiconductor with holes as majority charge carriers (net positive)
$Q$	Heat (energy) transfer
$Q_H$	Heat supply rate to TEGs
$Q_L$	Heat removal rate from TEGs
$R$	Electrical resistance
$R_c$	Electrical contact resistance
$\rho_p/\rho_n$	Electrical resistivity of the positive/negative TE elements
$\sigma$	Electrical conductivity

s (time)	Seconds
T	Temperature
$T_C/T_L$	Cold side or heat sink side temperature of TE module
$T_H$	Hot side temperature of TE module
$\tau$	Thompson coefficient
V	Volts
Voc	Open circuit voltage
W	Watts

## ABSTRACT

Waste heat recovery is a multi-billion-dollar industry with a compound annual growth rate of 8.8% assessed between 2016 to 2024 and low-grade waste heat ( $< 230^{\circ}\text{C} \pm 20^{\circ}\text{C}$ ) makes up 66% of this ubiquitous resource. Thermoelectric generators are preferred for the recovery process because they are cheap and are well suited for this temperature range. They generate power by converting thermal potential to electric potential, known as the Seebeck effect. Since they have no moving parts, they are inherently immune to mechanical failure or an intermittent need for maintenance. However, the challenge has been to effectively harvest waste heat with these modules to generate power, using passive processes. This work is focused on designing a device for optimized harvesting of waste energy from the ambient with a custom, evaporatively-cooled heat sink. This heat sink is designed to passively handle the cooling of the other side of the thermoelectric module so as to enable the attainment of a minimum of 5V, which is the minimum voltage required to power small mobile devices. The heat sink model is similar to a loop heat pipe but engineered for compactness. To ensure this level of efficacy is attained, several studies are made to optimize the wick. Non-metal wicks were considered as they do not contribute to an increase in temperature of the compensation chamber in loop heat pipes. A non-metal wick integrated with nanoparticles is tested and results show a clear thermal management enhancement over similar but virgin non-metal wicks, at over 16%. The heat source section of the device is optimized for energy-harvesting in low grade temperature regimes by incorporating a near-black body coating on the metal heat source section. Experimental results show that both the heat source and sink sections were able to induce sufficient thermal potential for the thermoelectric modules to passively generate up to 5V using eight 40mm by 40mm Bismuth Telluride modules in 3.5 minutes. The prototype is relatively cheap, inherently reliable and presents the possibility of passively harvesting low-grade waste heat for later use, including powering small electronic devices.

# CHAPTER 1. INTRODUCTION

## 1.1 Overview

A significant percentage of global energy use ends up as waste heat: efficient waste heat/ambient heat recovery and subsequent productive utilization has fascinated researchers over the years, with the advent of thermoelectric materials making the concept even more attractive [1, 2].

A Thermoelectric generator (TEG) converts an induced temperature differential on its sides into electricity. This is known as the Seebeck effect, where the Seebeck coefficient of a material is defined as a measure of the magnitude of induced thermoelectric voltage in response to an induced temperature difference across that material, denoted by  $\mu\text{V/K}$ . By exposing one side to ambient heat and cooling the other side with a suitable heat sink, a temperature differential is established, which the module converts to DC power.

The effectiveness of this conversion, however, greatly depends on the thermal management efficacy of the heat sink for the ‘cold-side’ temperature since waste heat fluxes are often in low temperature ranges (usually referred to as low-grade heat). Hence, the more efficient the cold side temperature, the more efficient the thermoelectric generator [3]. Muhammad, Ibrahim and Aziz [4] also emphasized this view recently, underscoring the potential of improving the performance of TEGs by refining the thermal management of the cold side.

Both active and passive heat sinks have been studied for cooling thermoelectric generators, including passive air [5-9], passive water [10,11], forced air [12-15], forced water [16-19] and heat pipes [20,21].

Passive heat sinks have no need of an auxiliary power source and contain no moving part, hence are intrinsically reliable. They may be less efficient than forced options [4], but are preferred when reliability, energy efficiency and compactness are all desired, as passive cooling options do not have auxiliary units that would take up space or require regular maintenance. These make passive

heat sinks very attractive for reliable, low-cost thermoelectric power generation. Passive heat sinks may be air/liquid-cooled by natural convection (sensible heat exchange), or liquid-cooled by latent heat absorption. The most potent is latent heat absorption, of which heat pipes are the most popular and effective. Passive cooling by latent heat absorption is also known as evaporative cooling.

Heat pipes and loop heat pipes are premier examples of evaporative cooling devices. They are efficient passive cooling devices that are based on the physics of latent heat absorption of liquids during phase change and may utilize single component fluids or zeotropes as the working fluid.

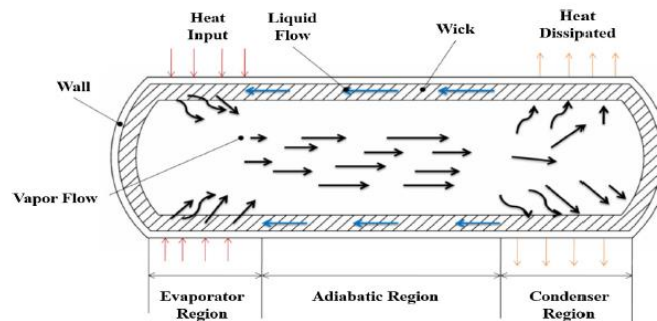


Figure 1: A heat pipe's working principle [22]

When in contact with a heat source, the fluid evaporates and, driven by a difference in vapor pressure, diffuses to the cooler end where it condenses thereby releasing the heat to the atmosphere, then recirculates back to the heat source by capillary action through a wick lining the internal surface area of the pipe. Basically, heat pipes utilize the physics of phase change to transport heat. During phase change, temperature is constant, and this allows the working fluid to absorb energy from a heat source without an equivalent rise in temperature.

Solid phase change materials are less efficient as the temperature distribution during melting is not uniform [23], and the latent heat capacity of vaporization is usually greater than latent heat of formation. However, heat pipes have two notable challenges, of which the most notable is fluid entrainment between the liquid and the vapor travelling in opposite directions through one delivery pipe.

The loop heat pipe is a variant of conventional heat pipes that eliminates the problem of entrainment by having separate delivery lines for the liquid and vapor streams. This makes it more reliable than conventional heat pipes.

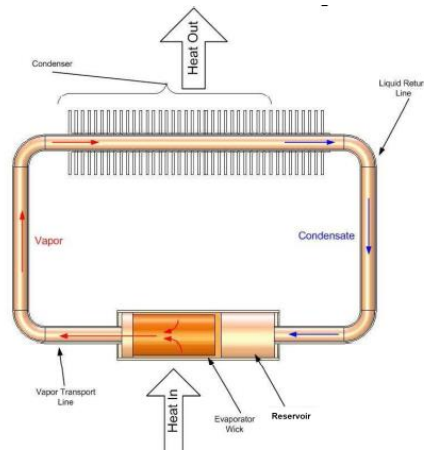


Figure 2: Loop Heat Pipe [24]

The operation of a loop heat pipe is based on the same physical processes as those of conventional heat pipes. The loop heat pipe consists of an evaporator area, a reservoir, a condenser area, and vapor and liquid transport lines. Only the evaporator and the reservoir contain wicks; the rest of the loop can be formed using smooth tubing, unlike traditional heat pipes [24].

The two major differences between loop heat pipes and a conventional heat pipes are the presence of the compensation chamber or reservoir and separate fluid transport lines for both fluid phases. The reservoir ensures steady fluid delivery and reduces the likelihood of burnout.

However, the heat pipe loop has several challenges too. The first is thermal leak to the reservoir through the highly conductive copper wick. [25]. Like heat pipes, loop heat pipes utilize a copper wick due to the metal's good capillary capability with water. This wick leads from the evaporator to the reservoir, hence conducts some heat from the evaporator straight into the reservoir, thereby increasing the sensible heat of the stored fluid, which affects the efficiency of the device.

Loop heat pipes are also lacking in compactness, and the various thermal resistances between the liquid and the main heat source would affect heat transfer. For example, in cooling an equipment,

the thermal transfer would have to go through a layer of metal. Also, if the contact between the metal and the heat source is not perfect, then micro air pockets could form in tiny cavities between the two surfaces, hence impede heat transfer. These challenges hamper thermoelectric power generation by limiting the obtainable temperature difference.

This has led several researchers to study the performance of non-metal wicks in loop heat pipes [26-28]. This resolved the challenge of thermal leak to the reservoir, but then non-metal wicks, like water, have poor thermal conductivity, which leads to uneven thermal distribution for the fluid in the wick in contact with the evaporator, and a localization of evaporating menisci [29]. Uneven thermal distribution in the radial direction through the wick may result in the formation of superheated fluid underneath the evaporator, which will adversely affect the efficacy of the heat sink. This is why non-metal wicks usually have a ‘boiling limit’ challenge.

One way of solving this challenge posed by non-metal wicks is the use of nanofluids. It is established by experimental evidence that nanofluids have better thermal conductivity than typical pure working fluids like water [30, 31]. This thermal enhancement is attributed to the Brownian motion of the nanoparticles within the fluid and increase in thermal conductivity due to the suspension of nanoparticles [32, 33]. However, running nanofluids as the working fluid of a loop heat pipe with non-metal wick would also induce thermal leak to the compensation chamber due to the enhanced thermal conductivity of the fluid.

To circumvent the challenge of thermal leak through the nanofluid itself, an innovative modification is hereby proposed: the immobilization of nanoparticles on both sides (top and bottom) of just the evaporator-section of a non-metal wick. This concept is hypothesized to enhance heat transfer to the working fluid, reduce the thermal resistance between the working fluid molecules and the evaporator section and induce negligible thermal leak to the reservoir fluid due to the inherent poor thermal conductivity of the other sections of the non-metal wick.

## 1.2 Objectives and Scope

The objective of this work is to design a heat sink capable of enabling a small array of  $\text{Bi}_2\text{Te}_3$  TEGs generate up to 5V by harvesting low-grade waste heat. Several studies have investigated the waste heat recovery potential of Thermoelectric generators including other waste heat recovery technologies like Organic Rankine Cycle, Kalina Cycle, ThermoPhotoVoltaic and Piezoelectric waste heat recovery technologies. To the best of the Author's knowledge, there has been no deliberate attempt to obtain usable power of a minimum of 5V for domestic use like powering small electronic devices through low-grade waste heat recovery using passively-cooled thermoelectric generators. This work is focused on the heat sink component of the thermoelectric power generation process. Thermoelectric modules have very low efficiencies, hence shrewd engineering design of the passive heat sink is required to obtain enough temperature potential to produce up to 5V under low-grade waste heat temperatures. The prototype will be cost-effective, portable, eco-friendly and safe for domestic use.

## CHAPTER 2. LITERATURE REVIEW

### 2.1 Thermoelectric Materials

A thermoelectric (TE) module is made up of n-type and p-type semiconducting materials. These semiconductor legs are uniquely connected such that they are thermally in parallel and electrically in series. The Semiconductors are materials whose electrical conductivity and band-gap ( $E_g$ ) range lie between that of conductors and insulators. The band-gap is the energy gap between the highest occupied molecular orbital (HOMO), known as the valence band, and the lowest unoccupied molecular orbital (LUMO), which is the conduction band of a material. TE materials can be broadly divided into organic and inorganic materials.

#### 2.1.1 Organic Thermoelectric Materials

These involve semiconductors that are mostly composed of carbon and hydrogen, together with oxygen, sulfur and nitrogen. An example is the iodine doped polyacetylene, reported to have attained a high conductivity due to the doping by Heeger and colleagues in 1977 [34-36]. The molecular structure of the semiconducting polymer dictates the electronic properties as they all depend on a conjugated carbon-carbon bonds system. This system enables the transport of electric charge through delocalized electrons. Due to an overlapping of the  $p$ -orbitals of neighboring atoms in such conjugated systems, the  $\pi$ -electrons are delocalized and, as a result, two molecular orbitals are formed: an empty antibonding orbital and a fully occupied bonding orbital. Increase in conjugation length leads to an increase in the energy bands formed by these molecular orbitals in a quasi-continuous form, only restricted by the band-gap [37].

#### 2.1.2 Inorganic Thermoelectric Materials

There are several families of inorganic semiconductors, and the classification is based on the structures and compositions of the materials. They include Half-Heusler, Clathrate, Silicide, Oxide, Chalcogenide and Skutterudite [38]. However, the family of inorganic materials under which Bismuth Telluride, the thermoelectric material used in this research, falls is Chalcogenides; specifically, Metal Chalcogenides.

### 2.1.3 Metal Chalcogenides

These contain one or more chalcogen atoms (S, Se, Te). They are quite diverse in structure, which translates to diverse physical and chemical properties. Metal chalcogenides are less ionic than their metal oxide counterparts, hence possess smaller bandgaps. Bismuth Chalcogenide, especially  $\text{Bi}_2\text{Te}_3$ , is one of the most popular metal Chalcogenides. Bismuth is a p-block metal, which includes other metals like Lead and Tin. Bismuth Telluride and its alloys are generally used for low temperature applications ( $<450\text{K}$ ) and have been commercially available since the 1950's [39-41]. Lead Telluride (heavily doped) have been used in RTG for years due to its effectiveness in temperatures ranging from  $600\text{K} - 800\text{K}$  [42,43]. For temperature ranges  $>1000\text{K}$ , rare-earth chalcogenides are very effective due to their high thermal stability [43]. The chalcogenides of these metals generally have low thermal conductivity and pliable electronic properties that can be modified for different operating temperature ranges [44-47]. All these properties make them very suitable for thermoelectrics. A more in-depth review on these Chalcogenides and others have been made by Sootsman et al. (2009), Zhao et al. (2016), Han et al. (2016) and Tan et al. (2016), to mention a few [46,48-50].

### 2.1.4 Bismuth Telluride Thermoelectrics

Bismuth Telluride is one of the most well-known type of thermoelectric materials and is best suited for use in low and medium temperature applications, which is the expected temperature range for this research. It is also less expensive than other thermoelectric material due to its mass production and extensive variety of usage [51].  $\text{Bi}_2\text{Te}_3$  is a gray semiconductor with a small bandgap and a trigonal unit cell. Van der Waals bonding between neighboring tellurium atoms accounts for the ease with which  $\text{Bi}_2\text{Te}_3$  sticks along its trigonal axis. Consequently,  $\text{Bi}_2\text{Te}_3$  and its alloys used for cooling or power generation have to be polycrystalline [52].

### 2.1.5 Figure of Merit (zT)

A thermoelectric couple consists of a pair of n-type and p-type legs. A number of such couples connected in series makes a thermoelectric module. An electrical insulator, usually a ceramic, is used to cover these couples and their electrical interconnects [53]. Thermoelectric material properties are very sensitive to temperature and this has to be considered when choosing materials

for a specific operation. Each thermoelectric material has a temperature range of operation outside which its performance falls drastically.

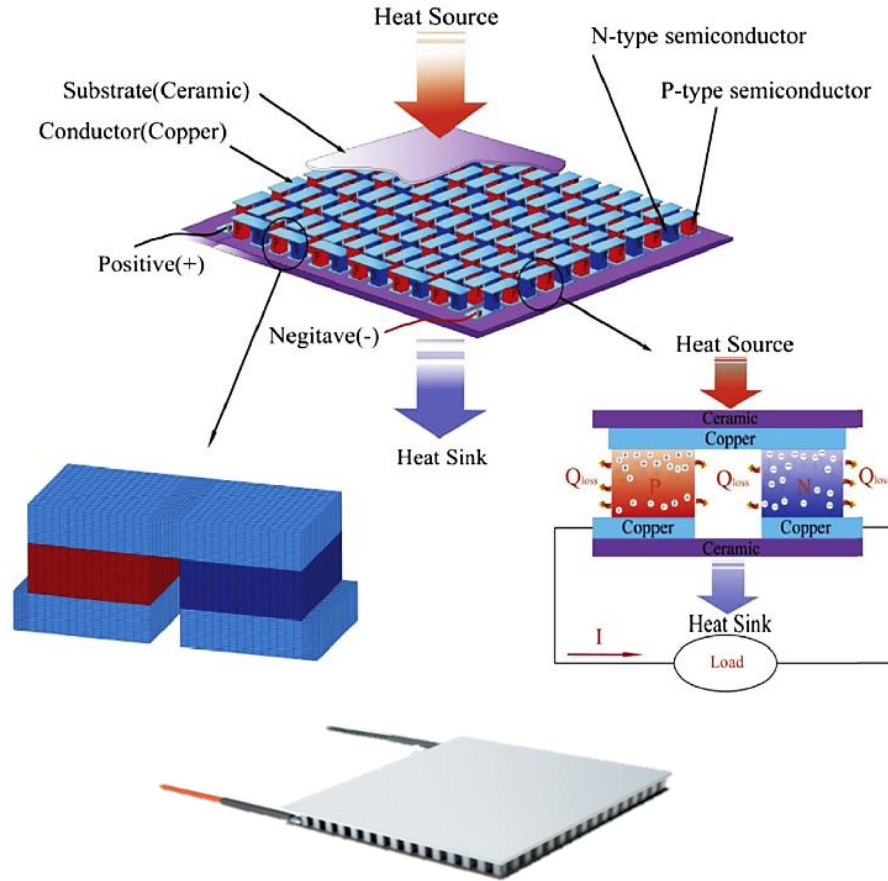


Figure 3: Thermoelectric module showing p and n semiconductor legs arranged in series [54], and an actual 40mm x 40mm Bi<sub>2</sub>Te<sub>3</sub> thermoelectric module below.

This figure of merit,  $zT$ , is a property that describes and quantifies the performance of a thermoelectric material. It is dependent on the thermoelectric material properties like thermal conductivity  $\kappa$ , Seebeck coefficient  $\alpha$  and electrical conductivity  $\sigma$ , such that  $zT = \frac{\alpha^2 \sigma T}{\kappa}$ , where  $S = \Delta V / \Delta T$  ( $\mu V / K$ ) and  $T$  is the temperature of the material. The equation for  $zT$  reveals that the conversion efficiency of thermoelectrics can be improved by increasing the Seebeck coefficient and electrical conductivity while lowering the thermal conductivity [55]. But then, it is difficult to increase the thermal conductivity of a material without increasing its electrical conductivity.  $\kappa$ ,

however, can be reduced by adjusting the material property such that it experiences a high degree of phonon scattering (like a glass, hence lowering " $\kappa$ "), and the reverse for the electrons (like a crystal, hence maintaining  $\sigma$ ), as proposed by G.A. Slack in Rowe, 2005 [56]. Generally, for good efficiency, a low ratio of  $\kappa_{\text{phonon}}/\kappa_{\text{electron}}$  is desired.

Depending on the temperature range of an operation, different classes of thermoelectric materials can be used -- Bismuth Telluride-based materials, Silicon-Germanium alloys and Lead Telluride-based materials. The variation of the Seebeck coefficient and the electrical conductivity of these heavily doped semiconductors, as a function of the reduced Fermi energy, serves for the optimization of the power factor,  $\alpha^2\sigma$  [57].

Bismuth Telluride-based materials are reported to have the highest figure-of-merit ( $3.4 \times 10^{-3} \text{ K}^{-1}$ ) but their operation is restricted to low temperature ranges, typically below 500K. Lead Telluride follows closely at an averaged figure-of-merit of  $2.0 \times 10^{-3} \text{ K}^{-1}$ , thriving at mid-range temperatures of about 600K -- 800K. Silicon Germanium alloys have the least figure of merit of the three, with  $0.8 \times 10^{-3} \text{ K}^{-1}$  but is the most thermally stable, being able to operate for extended periods of time at temperatures over 1000K [58–62].

With recent advances being made in material science with respect to understanding the physics of phonon scattering and energy filtering, promising development of Nanocomposites with the capacity for much higher figures of merit have been reported [63]. For example, the Tellurium-based glasses with high copper concentrations are confirming Chalcogenide semiconducting glasses for high-performance thermoelectric materials [64].

These new generation of binary and ternary chalcogenides possess complex structures and very low  $\kappa$ , hence offering a new outlook on designing high performance thermoelectric materials [38]. For example,  $\text{La}_{3-x}\text{Te}_4$  can attain a  $zT$  value of approximately 1.2 at 1300 K [65,66]. In 2014, SnSe was reported to have attained an unprecedented  $zT$  of 2.6 at 923 K in single crystal samples due to its structural anisotropy and ultralow  $\kappa_{\text{phonon}}$  [67].

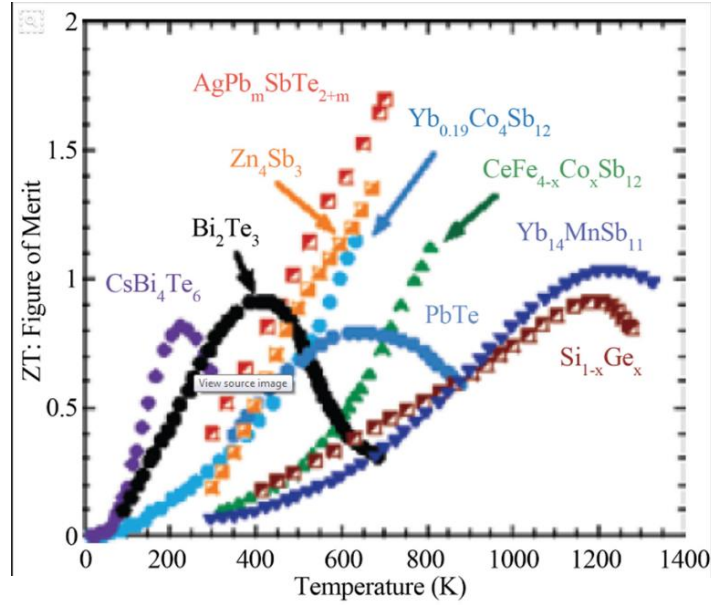


Figure 4: Figure of Merit ( $zT$ ) as a function of temperature for several high-efficiency bulk thermoelectric materials [68].

Many other ternary chalcogenide systems with complex structures and ultralow  $\kappa_{\text{phonon}}$ , hence an overall lower value of the thermal conductivity, have been reported. Quite a number of these are known to have  $zT$  values greater than 1.0, like  $\text{CsAg}_5\text{Te}_3$  [69],  $\text{AgBi}_3\text{S}_5$  [70], and  $\text{K}_2\text{Bi}_8\text{Se}_{13}$  [71].

## 2.2 Thermoelectric Effects

For thermoelectric modules generally, the thermodynamic conversion of heat to work involves four unique processes. Of these, two are irreversible while the other two are reversible. The reversible processes are Seebeck/Peltier and Thomson effects [38]. The irreversible processes are the Fourier effect, which accounts for heat conduction, and the Joule effect, which accounts for electrical resistance. The Seebeck and Peltier effects are actually two physically relative effects in that where a temperature difference across a module leads to electric power generation in the Seebeck effect, the input of electric power -- hence an imposition of potential difference across the module -- leads to the generation of a temperature difference on both sides of the module, known as the Peltier effect [72].

Thus, thermoelectric modules or devices can convert electrical energy into thermal energy and vice versa. This ability is based on the fact that temperature differences can set charge carriers in motion (Figure 5).

When a material is kept between two different temperatures, an open-circuit voltage is generated. The Seebeck coefficient  $\alpha$  ( $\mu\text{V/K}$  or  $\text{V/K}$ ) is a property of the material that relates the generated open-circuit voltage ( $V$ ) with the temperature difference  $\Delta T$  (K) that brought about the voltage generation [72], thus:

$$V_{oc} = \alpha \Delta T \quad (1)$$

So,

$$\alpha = V_{oc}/\Delta T = |\alpha_p| + |\alpha_n| \quad (2)$$

where  $|\alpha_p| + |\alpha_n|$  refers to the effective Seebeck coefficient of the semi-conducting materials [30].

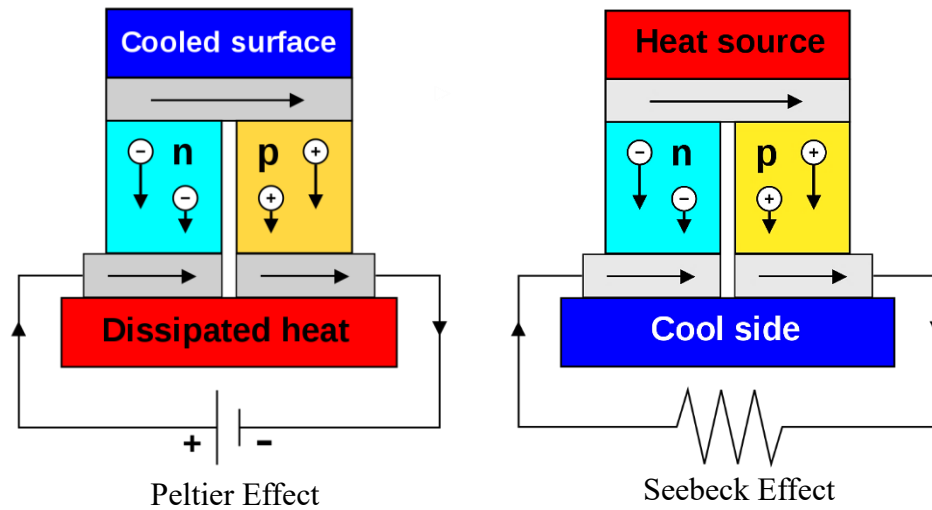


Figure 5: Seebeck and Peltier effects [73]

For the Peltier effect, where passing a direct current through a circuit of dissimilar metals leads to the rejection or absorption of heat depending on the direction of the current,

$$P_p = \pi I = \alpha I T_c \quad (3)$$

where  $\pi$  (V) is the Peltier coefficient and  $T_c$  is the cold-side module temperature [38].

For the irreversible effects – the Joule heating effect and the Fourier effect, they are expressed as follows,

$$P_J = I^2R/2 \quad (4)$$

as the Joule effect [30]; and,

$$P_F = k\Delta T \quad (5)$$

as the Fourier effect.

The Thomson effect, however, is usually neglected as its coefficient is quite difficult to obtain experimentally and its value is considered negligible compared to Joule heating [72]. The Thomson effect is expressed as,

$$P_T = \tau I \Delta T \quad (6)$$

where  $\tau$  (V/K) is the Thomson coefficient [38], expressed as:

$$\tau = (T_{avg}d\alpha)/\Delta T \quad (7)$$

### 2.3 Thermoelectric Generators

A simple schematic of a TEG is shown in Figure 6, showing the two dissimilar materials, p and n semiconductors, connected thermally in parallel and electrically in series [38]. Heat is supplied on one side, leading to a temperature  $T_H$ , while the other side is maintained at a lower temperature  $T_L$  by a heat sink. Due to the imposed temperature difference, a current,  $I$ , flows through an external load resistance as shown in Figure 6 [38].

The power output of a TEG depends on the material properties of the semiconductor, the heat sink, the temperature difference, and even the external load resistance [74]. The heat sink is very important in that it is more crucial for obtaining higher temperature potential, hence more power output, than the heat source. Besides this being true in cases where the heat source is constant or cannot be easily increased or controlled, increasing the heat source in a TEG with an inefficient heat sink will not lead to an increase in temperature potential as the heat rejection has to be effective for the TEG to remain viable or efficient.

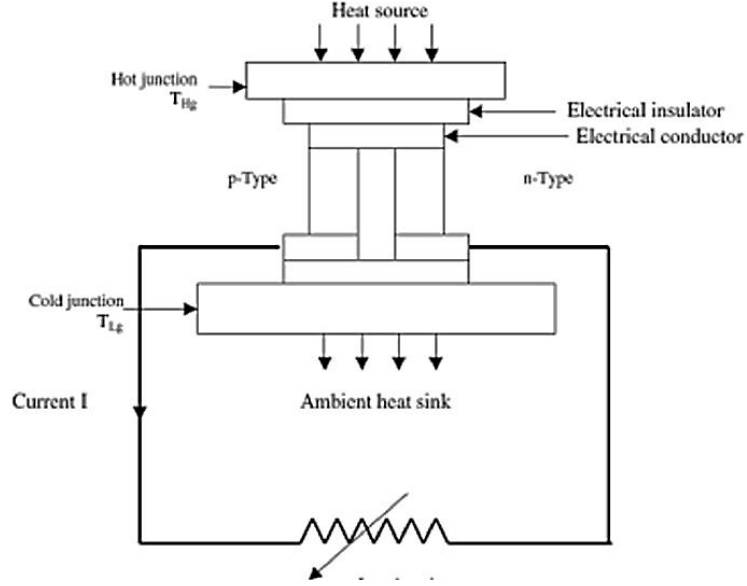


Figure 6: Schematic of a TEG [74]

Equations for the heat supply and heat removal rate, power output and thermal efficiency are as follows:

Heat supply rate to the thermoelectric generator [74]:

$$Q_H = \alpha IT_H - 0.5I^2R + \kappa(T_H - T_L) \quad (8)$$

Heat removal rate of the thermoelectric generator [74]:

$$Q_L = \alpha IT_L + 0.5I^2R + \kappa(T_H - T_L) \quad (9)$$

Where  $R$  is the electrical resistance of the semiconductors. Conversely, for a Peltier device, the heat removal or cooling rate would be given by  $Q_L = \alpha IT_L - (0.5I^2R + \kappa(T_H - T_L))$  [30].

When the electrical contact resistance ( $R_c$ ) between p and n couples is considered, equations (8) and (9), respectively, become [74]:

$$Q_H = \alpha IT_H - 0.5I^2R + \kappa(T_H - T_L) - I^2R_c \quad (10)$$

$$Q_L = \alpha IT_L + 0.5I^2R + \kappa(T_H - T_L) + I^2R_c \quad (11)$$

While the power output and thermal efficiency are respectively given by [38]:

$$P = \alpha I(T_H - T_L) - I^2R \quad (12)$$

$$\eta_{th} = P/Q_H \quad (13)$$

When  $dP/dI$  is equated to zero, the result is the optimum value of  $I$  [75]:

$$I_{opt} = [\alpha(T_H - T_L)]/2R \quad (14)$$

The power output from a thermocouple is found to be proportional to its area and inversely proportional to the length. Hence, reasonable conversion efficiency can be attained by a large number of short-legged thermocouples [58]. Generally, the overall performance of a thermoelectric device depends on the device heat source and sink components, and on the material properties of the thermocouples [76].

### 2.3.1 Advantages and Applications of Thermoelectric Generators

Thermoelectric generators hold a lot of promise, with the potential of substantially reducing our use of fossil fuels by minimizing energy consumption, which also protects our environment. A thermoelectric generator is a thermoelectric module under the influence of the Seebeck effect. TEGs can be seen as heat engines in which charge carriers serve as the working fluid. Being a solid-state device, they are silent in operation, have no moving parts and are very reliable [77].

Table 1: Advantages of Thermoelectric Modules

• No moving parts, hence no maintenance	• Eco-friendly. Recycles waste heat
• Compact and lightweight; silent operation	• Scalable
• Very reliable (MTBF of over 100,000 hours)	• Heating and cooling can be obtained by reversing DC Power polarity.

The core of any TEG is the thermoelectric module, which are commercially available, notably  $\text{Bi}_2\text{Te}_3$ . So long as a temperature difference is maintained across the thermoelectric module, electric power can be delivered to an external load by virtue of the Seebeck effect. To achieve this difference, heat is supplied on one surface while a heat sink is used on the other surface to provide cooling where the heat is rejected. The heat supply can be from via a variety of sources and can be active like the hot surface of a machinery or vehicle exhaust pipe, or passive like solar heating/ambient temperature or body heat [58,59].

Due to the several desirable physical properties of thermoelectric devices, like its solid state, size and weight, they enjoy a wide range of applications in different industries [78]. Although currently, the generally less-than-stellar efficiency of thermoelectric devices restricts its potential utility reach, TEGs are still being used in specialized medical, military, and space applications [76,77].

Tracing its humble utility beginnings to a kerosene lamp, including being used in a wood stove to generate electricity to power small fans and low-wattage light bulbs [79–81], other use cases of the thermoelectric generator in recent times include applications in aerospace, medical services, electronic devices, industrial utilities, transportation tools and temperature detecting and measuring facilities [76]. Thermoelectric devices can act as thermal energy sensors coolers or power generators and are used in many fields like in the military, biology, aerospace, medicine, instrument and industrial or commercial products [78].

Thermoelectric generators can also convert solar energy to electricity as an alternative or support to Photovoltaic technology. They are also the only system that can easily and effectively harvest waste heat from the ambient or any other source and convert it directly to power. Being able to harvest waste heat up to 5V would make it possible to power small electronic devices like mobile phones in places that are off-grid by design or accident, or in countries or states with erratic electric power supply. This technology can also be used in niche fields such as space missions to distant planets [82] as thermoelectric devices have an MTBF of over 11 years.

## **2.4 Cooling Techniques for Thermoelectric Generators**

For a TE module with a known and constant material property, the only way to enhance its efficacy in waste heat harvesting is to optimize the heat sink effectiveness. In waste heat harvesting, the heat source is usually low-grade heat, usually under 500K. Hence, a good heatsink is the only way to maintain the effectiveness of any TEG in harvesting useable power.

Improving the thermal management of a TEG has the theoretical potential of increasing its thermoelectric conversion efficiency by 5% -- 10% and experimental results suggest it could be even more [83,84]. This shows how important the heat sink section of a TEG is to the overall

effectiveness of the device in harvesting waste heat. For example, in a study by Weidenkaff *et al.* (2013), they observed that insufficient cooling from their heat sink at higher heat fluxes resulted in a 15% drop in voltage production compared to expected values [85].

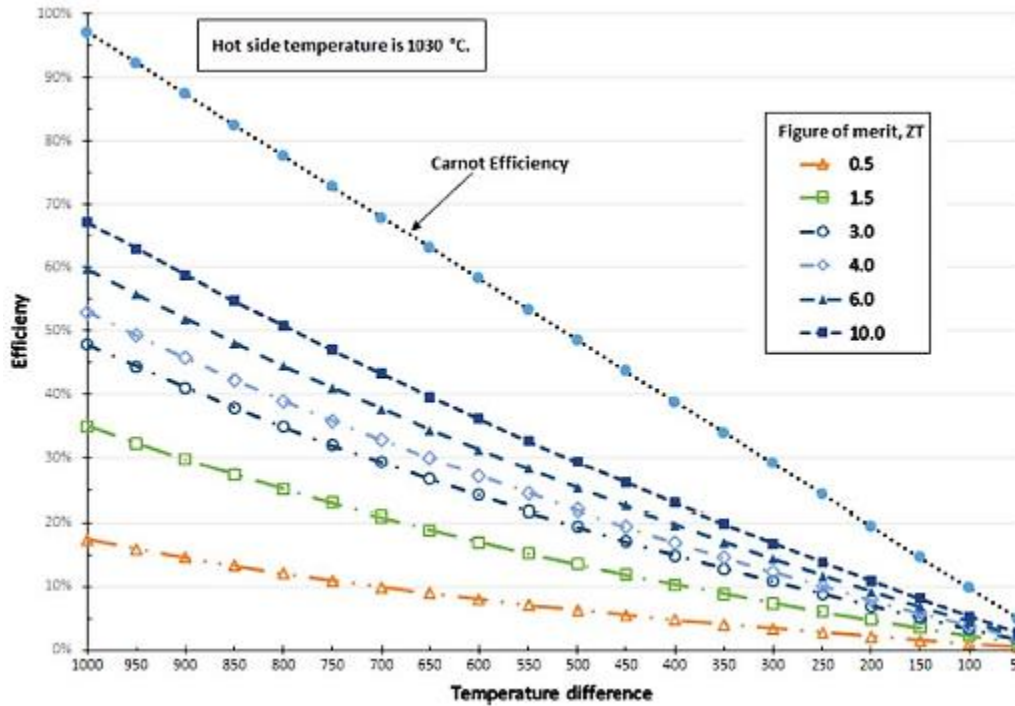


Figure 7: Effect of increasing cold side temperature on thermoelectric efficiency for a hypothetical hot side temperature of 1030°C [4].

### 2.4.1 Active and Passive Heat Sinks

Heat sinks may be active or passive. Active heat sinks use electric power, like fans or water pumps. Passive heat sinks need no power input for operation, like metal fins and evaporative cooling units. Active heat sinks are usually more effective than passive heat sinks and can become imperative in high heat flux systems, but they reduce the overall COP of the system since the power input to the heat sink increases the overall power input required for sustaining the cooling power being supplied.

Active heat sinks use forced convection to pump away heat using air or water. Air or water are usually used because they are ubiquitous, easy to use, cheaper than other working fluid options, non-toxic, non-corrosive and ecofriendly.

Forced air cooling using fan(s) has been well studied under transient and steady state heat sources, with a focus on optimization [86-89]. Mastbergen and Willson [90] presented a prototype TEG with forced air-cooling for the cold side using a 1W fan. The device was able to generate up to 4W, sufficient to power an array of high intensity LEDs.

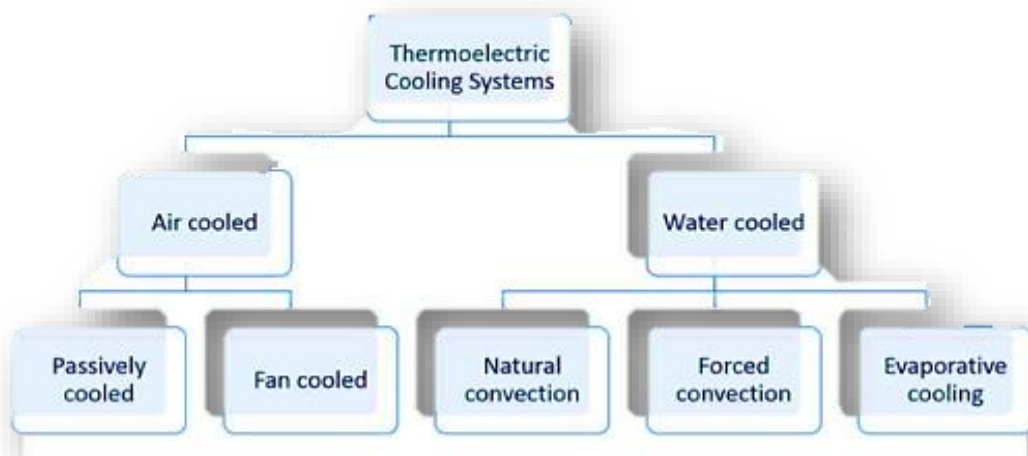


Figure 8: Classification of TEG cooling technologies

Also, waste heat recovery in the automotive industry using fan-cooled TEGs is well documented [91-95]. Hsu *et al.* [94,96] studied a range of heat sink configurations while using forced air. Three configurations with ten, twenty-two and forty-four fins in their heat sinks, respectively, were investigated so as to find the optimal configuration. With the cold side temperature of the TEG at 343.7K and an average temperature difference of 88.3K, their system generated a peak power of 44.13W, indicating a maximum conversion efficiency of 2.1%. Gou *et al.* [88] reported a similar efficiency while using forced air cooling on a TEG for industrial waste heat recovery. They were able to restrict the maximum increment in cold side temperature to 14K and cited irreversibility in heat transfer as a challenge in the thermal enhancement of the cold side temperature of TEGs.

Forced water cooling systems for TEGs are currently the most widely used, from combined heat and power generation industries to automobiles [4], despite the prominent disadvantage of pumping cost. Niu *et al.* [97] and Chen *et al.* [98] constructed an experimental TEG unit for a study that included the effects of the hot and cold fluid inlet temperatures and flow rates on power output and conversion efficiency. Both researchers concluded that the performance of the TEG depended more on the inlet temperature of the cooling fluid besides the flow rate of the heating fluid, with Niu *et al.* achieving values like 4.44% conversion efficiency and 146.5W power output with the inlet fluid entering at 30°C and a temperature difference of 120°C. Solar energy harvesting using TEGs and active water cooling has been widely studied [99-104]. For example, using a microchannel heat sink, Fan *et al.* was able to cool a TEG unit to produce 4.9W at 2.9% electrical efficiency with a 109°C temperature difference [104].

Many of these studies do not consider the parasitic losses incurred in the pumps, piping and water-to-ambient heat exchangers [4]. To minimize auxiliary power consumption thermoelectric generators using forced water cooling, A predictive computational model of a TEG waste heat dissipation system was developed and tested by Aranguren *et al.* [105,106]. Their model established that the optimization of cooling system parameters like flowrates, piping and secondary heat exchanger could increase the obtainable power by as much as 40% at maximum efficiency [4].

#### **2.4.2 Passive Cooling Systems for TEGs**

Passive cooling systems make use of natural convection and has the advantage of having no parasitic power consumption unlike active cooling systems. However, they are generally less effective than active heat sinks in thermal management. As a result, natural convection cooling of TEGs with water or air has received less attention in past studies than its active cooling variant. Champier *et al.* [107] designed a system to simulate a process where the cold side of a TEG would be maintained by water in an aluminum tank while the hot side would be maintained by heat extracted from the exhaust air from a biomass stove using aluminum fins. According to the design, the water in the Aluminum tank could be used for domestic warm/hot water use as heat is pumped into it over time. The system was able to extract up to 9.5W from the TEG for an almost matched load.

Since water and air are naturally poor conductors of heat, the increasing dependence on their ability to conduct away heat is the main reason passive cooling systems are less effective. With active cooling, the high Nusselt number usually involved implies that convection is the dominant medium of heat transfer. However, in passive systems, the Nusselt number is much lower and quite close to 1. An example is the experiment with stagnant water as the heat sink or when the TEG is air cooled by the ambient on a still day. In such cases, the thermal management of the TEG becomes very dependent on the conductivity of the working fluid. To minimize the severity of this, metal fins, evaporative cooling or working fluid thermal enhancement using nanofluids have been explored.

Metal fins and evaporative cooling boast much higher conductivities than air or pure water and work to pump the heat away from the TEG to a different location where it can be released to a reservoir. Evaporative cooling, however, has a much higher conductivity than metals due to the relatively high heat capacity of water and the high heat transfer coefficients of boiling and condensation. For example, a long heat pipe can approach an effective thermal conductivity of 100KW/mK or more, compared to copper that is just about 0.4KW/mK.

Metal fins may be restricted by the conductivity of the metal in use, but it must be noted that both metal fins and evaporative cooling still depend on the heat transfer conditions at the reservoir to remain effective. Ozeh and Nnanna (2018) reported an underwhelming thermal management performance for a heat pipe in still air compared to the same heat pipe with less than 1m/s air velocity [108].

### **2.4.3 Evaporative Cooling using Heat Pipes and Nanofluids**

Evaporative cooling takes advantage of the high latent heat of vaporization of water to provide cooling to the TEG using a heat pipe or a related thermo-syphoning device [4]. Date *et al.* [109] conducted a comparative study of different cooling systems like bare plates, heat pipes and cooling fins and found that heat pipes had the most effective thermal management capability.

Some heat pipes use a wick to transport condensed working fluid back to the evaporator while some make use of gravity or centrifugal force. Nuwayhid and Hamade [110], using a wickless,

loop configuration on the cold side of a TEG in which the working fluid is returned mainly by gravity, were able to achieve 3W of power for a temperature difference of 70°C–80°C at a cold side temperature of over 100°C, which leaves a lot to be desired from the thermal management of the system.

Djafar *et al.* [111] reported a 400% to 600% increase in power produced from TEGs from using a heat pipe on the cold side of a TEG compared to natural convection of air without a heat pipe. Evaporative cooling of TEGs using heat pipes have been investigated with solar collectors as heat source [112,113], and in automobiles [93]. In automobiles, the TEG was used to replace the conventional radiator, providing a combined power of 75W at 2.1% device efficiency when employed in a 2L engine of passenger car [4,93]. During the test, the vehicle was driven at 80km/h, implying the advantage of heightened convective heat transfer coefficient from the fins of the heat pipe, which led to a considerably higher thermal performance than a conventional radiator.

Most heat pipes make use of a metal wick to return condensed working fluid to the evaporator, with water as the usual working fluid in such cases. However, the thermal management of heat pipes is restricted by several working limitations, like the entrainment limit, capillary limit, boiling limit and viscous limit. The viscous limit and capillary limit are related to pressure difference challenges while the boiling limit is a heat flux challenge. However, entrainment is primarily a design challenge than a heat flux challenge and that was remedied with the development of loop heat pipes.

Loop heat pipes have separate liquid and vapor transport systems and a reservoir. The separate lines eliminate the possibility of entrainment while the presence of a working fluid reservoir for the wick, situated close to the evaporator, prevents the possibility of burnout, effectively eliminating capillary limit challenges. However, there are reports of thermal leak to the reservoir via the highly conductive copper wick in contact or near contact with the hot evaporator, also witnessed in an experiment conducted by Ozeh and Nnanna [108] where the reservoir of an Aluminum metal wick revealed a significant increase in temperature compared to negligible temperature change for a non-metal wick. The consequence of this backflow of heat from the evaporator through the metal wick is ultimately the same as that of the challenge of boiling limit,

where the temperature rise in the entire system causes the working fluid to boil and evaporate before they get to the evaporator: both cases of thermal leak and boiling limit ultimately lead to burnout. But where boiling limit has a heat flux threshold below which it is inconsequential, thermal leak to the reservoir is parasitic and occurs at all working temperatures, increasing with increase in heat flux.

These limitations hamper thermoelectric power generation by limiting the obtainable temperature difference [108] and has led several researchers to study the performance of non-metal wicks in loop heat pipes [26-28]. This resolved the challenge of thermal leak to the reservoir, but then non-metal wicks, like water, have poor thermal conductivity, which leads to uneven thermal distribution for the fluid in the wick in contact with the evaporator, and a localization of evaporating menisci [108,29]. Uneven thermal distribution in the radial direction through the wick may result in the formation of superheated fluid underneath the evaporator, which will have a negative impact on the thermal management of the TEG.

The use of Nanofluids have been explored as a way of increasing the thermal transport capability of working fluids that are naturally poor thermal conductors, like water. Metal or metal oxide nanoparticles suspended in a fluid can increase the thermal responsiveness of the fluid. In their study, Nnanna *et al.* asserted this enhancement over the base fluid based on experimental evidence [30]. In an earlier study by Nnanna (2007) on an experimental model of temperature-driven nanofluid, the superiority of the thermal conductivity of nanofluids over an ordinary working fluid like water was underscored [31]. This thermal enhancement is attributed to the Brownian motion of the nanoparticles within the fluid and increase in thermal conductivity due to the suspension of nanoparticles [32, 33].

However, running nanofluids as the working fluid of a loop heat pipe with non-metal wick would also induce thermal leak to the compensation chamber by virtue of the enhanced thermal conductivity of the fluid. Furthermore, it is unclear how long the nanoparticles will stay suspended in the working fluid for a prolonged use cycle of evaporation and condensation. In designing a heat sink for passively harvesting up to 5V with TEGs, this research presents a novel perspective

in this area by enhancing the thermal responsiveness of the non-metal wick through immobilizing metal-based nanoparticles on it, instead of using a nanofluid.

Although the Brownian motion effect is lost when nanoparticles are immobilized on a solid substrate, which would lead to less thermal enhancement capability compared to freely moving nanoparticles in fluids, the nanoparticles are hypothesized to contribute their superior thermal conductivity to the integrated wick-water system from their immobilized positions on the wick, and by localized thermal spreading around each particle in the working fluid, lead to an overall heightened thermal responsiveness of both the wick and the working fluid. This also eliminates the concern of the suspended nanoparticles settling out of the working fluid after prolonged use.

## CHAPTER 3. RESEARCH METHODOLOGY

### 3.1 Materials and Preliminary Tests

The materials involved in this study are thermoelectric modules, a Polyethylene wick, Deionized water and a ~1.7mm thick Aluminum 3003 H14 metal sheet with a thermal conductivity of approximately 180W/mK and a Young’s modulus of 70 GPa [114]. The nanopowders used in this study are 20nm Aluminum Oxide Nanoparticles ( $Al_2O_3$ , gamma, 99+ %) with a density of 3980kg/m<sup>3</sup> and 30nm Copper Nanoparticles (Cu with 5.2wt%  $Cu_2O$ ) with a density of 0.25g/cm<sup>3</sup>.

#### 3.1.1 The Thermoelectric modules

The Thermoelectric modules are commercially available Bismuth Telluride ( $Bi_2Te_3$ ) TEC1-12706 thermoelectric modules with a dimension of 40mm x 40mm x 3.9mm. Other properties of the modules are shown in Table 2.

Table 2: Properties of the  $Bi_2Te_3$  modules

Term	Unit	Value
Type of material		$Bi_2Te_3$
$\alpha_n = \alpha_p$	V/C	$\pm 2E-04$
$\rho_n = \rho_p$	$\Omega m$	$1E-05$
K	W/mC	1.50
$A_p/A_n$		1
$A_n = A_p$	m <sup>2</sup>	$1.17E-05$
$D_n = D_p$	m	0.0039
$L_p = L_n$	m	$4.49E-03$
$ \alpha $	V/C	$4E-04$

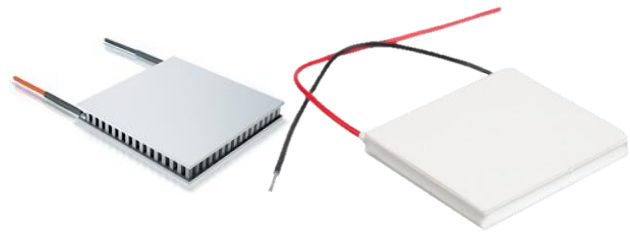


Figure 9: The  $Bi_2Te_3$  TEC1-12706 thermoelectric modules

### 3.1.2 The Wick

The wick is a hydrophilic, Porex® Polyethylene (PE) wick purchased from Interstate Specialty Products and has an average median pore size of  $\approx 19\mu\text{m}$ .



Figure 10: The PE wick

#### 3.1.2.1 Immobilization of nanoparticles on the wick

At first, to produce the nanoparticle-immobilized wick, the section of the wick's surface for the immobilization is roughened and punctured with needle within the confines of the section, as uniformly as possible, before introducing the nanoparticle suspension. The procedure followed for the Alumina goes thus:

- The wick, which is the substrate, is cleaned, then the surfaces of interest roughened (scratched/mechanically etched). The lacerations on the roughened surfaces, however, are sparse so as not to compromise the integrity of the wick. The surfaces of interest are both sides of the wick in direct contact with the hot side of the thermoelectric modules.
- Micro-punctures are made on both roughened surfaces with a 0.65mm needle.
- The solvent is 50%:50% DMAc:H<sub>2</sub>O. The DMAc concentration is thus minimized to inhibit its evaporation during sonication and to make the solvent less concentrated -- enough to have a softening effect on the plastic but not to denature it.
- The required percent weight of Al<sub>2</sub>O<sub>3</sub> nanoparticle per weight of solvent is thereafter carefully measured under a fume hood, mixed with the solvent and sonicated for at least 30 minutes with an ultrasonicator at 0.5 cycle, 50 amplitude.

- The wick is wrapped with a non-permeable material, leaving only the surfaces of interest exposed; then introduced to the solvent and dipped repeatedly for 20 – 30 minutes.
- Curing is carried out in an oven at 38°C for 2.5 - 3 days.

For the Cu nanoparticle, the only differences from the procedure above are:

- (1) The solvent is just water; no DMAc is used.
- (2) The sonication is extended to 2 hours as Cu nanopowder was observed to have less stability in water than Al<sub>2</sub>O<sub>3</sub>.

Sonication, however, had negligible effect on the Cu nanoparticles, unlike Alumina. Furthermore, the objective was to introduce the nanoparticles to the wick, thereby obtain an integrated solid material, not to keep the nanoparticles in a solution, which is the chief objective when sonicating nanoparticle solutions. Vigorously shaking the Cu nanoparticles in carefully measured DI water solvent led to a much more uniform suspension for the immobilization process on the wick.

It was also discovered that both roughening the surface of the wick and allowing the wick to dry out completely after immobilization severely affected its hydrophilicity by restricting capillarity and permeability. Future tests did not include any form of laceration on the wick surfaces and it was ensured the immobilization step was the final step before any experiment with the wick so as to prevent it from drying up before use.

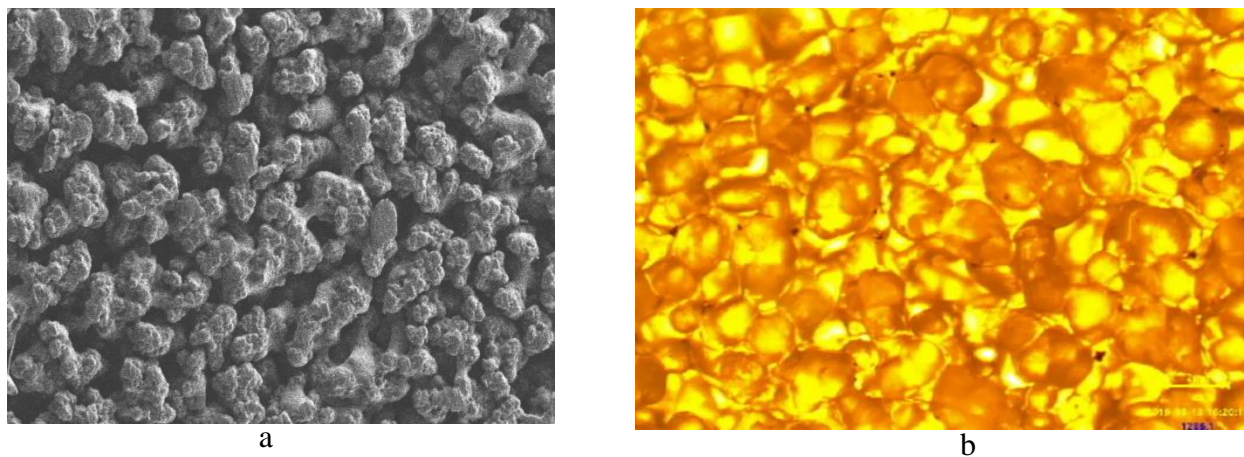


Figure 11: (a) SEM image of plain PE wick before immobilization; (b) A 20-micron view of the wick under a microscope after immobilization. The red dots are the nanoparticles attached to the walls of the wick.

### 3.1.2.2 Porosity, Effective Conductivity and Capillarity of the wick

The porosity, effective conductivity and capillarity of the wick were experimentally obtained. To obtain the porosity, a measured section of the wick was cut out and weighed. The cut-out section was then saturated with the working fluid (DI water) and weighed again. From the difference in mass and with the density of water known, the volume of water in the saturated wick section was calculated. From the dimensions of the wick, the apparent volume of the wick was determined. A ratio of real to apparent volume gives the fraction of wick volume occupied by the fluid – the porosity.

The effective conductivity of the wick after immobilization is an important factor in determining the boiling limit of the wick. After immobilization, it is expected that the thermal conductivity will be different and greater than the thermal conductivity of a plain PE wick. The setup below was used to determine the thermal conductivity of the integrated wick:

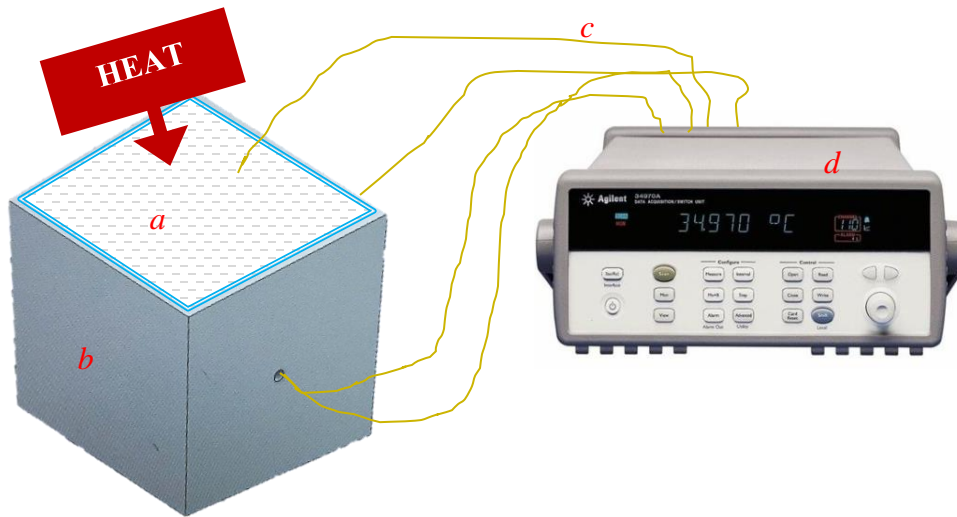


Figure 12: Setup for finding the effective conductivity of the wick. **'a'** is the integrated wick; **'b'** is a thermal insulating vessel containing water; **'c'** are thermocouples attached to the top and bottom of the wick, and inside the vessel to measure the change in temperature of the water; **'d'** is a data acquisition unit.

When heat is applied to one side of the wick, the energy flows across the wick to the water and soon the water temperature begins to rise.

Using  $Q = mC\Delta T$ , the thermal energy transfer to the water can be calculated. Then with Fourier's law,  $Q = kA \frac{\Delta T}{\Delta x}$ , the conductivity of the integrated wick,  $k$ , is determined; where  $A$  refers to the area of the wick in contact with heat,  $\Delta x$  is the thickness of the wick and  $\Delta T$  is obtained from the thermocouple measurements for the top and bottom of the wick.

Capillarity is one of the most important properties of any wick, especially when the orientation of the heat sink is against gravity by design. The lesser the pumping power, the more difficult it would be for the working fluid to return to the evaporator, which would eventually lead to dry out. To determine the capillarity of the wick, a strip of the wick was cut off and positioned adjacent a ruler and the rate at which working fluid traveled up from the bottom of the wick was recorded with a cellphone video camera (Fig. 13).

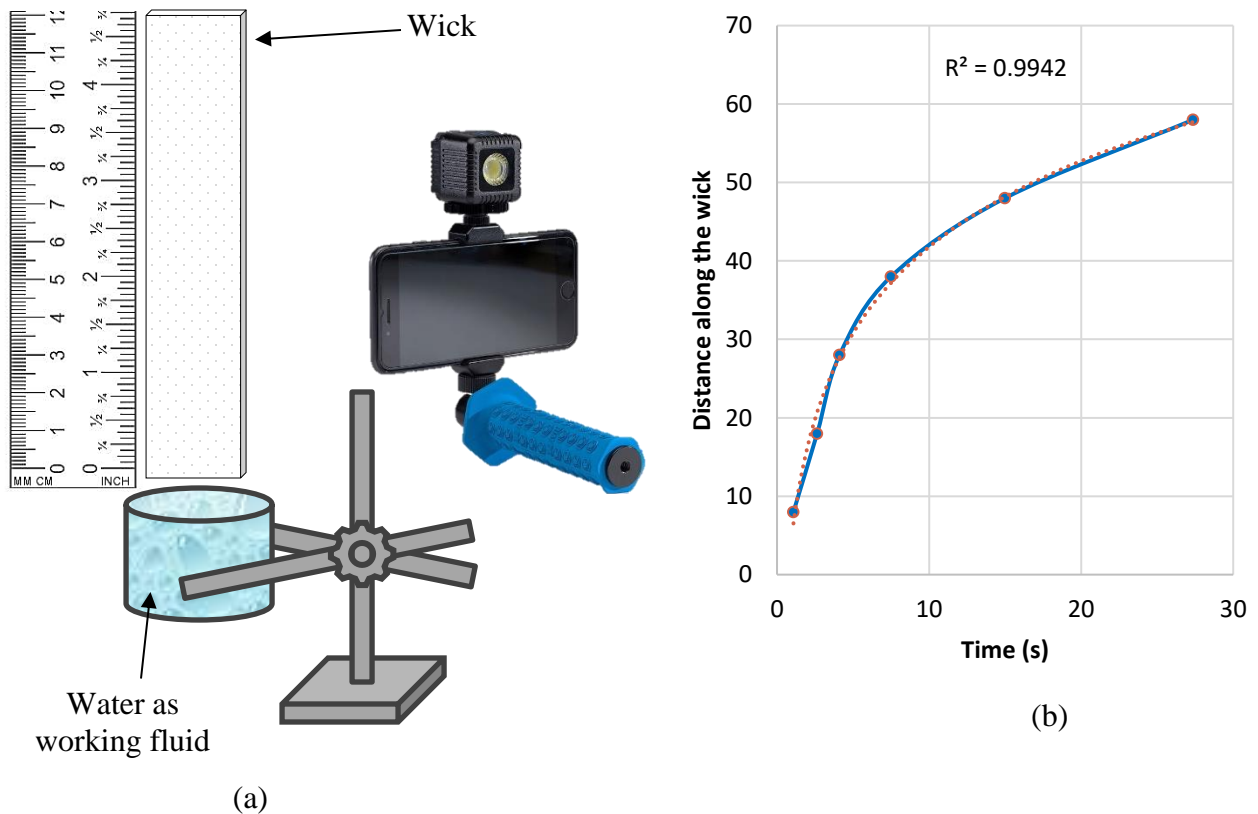


Figure 13a, b: To determine the rise (m/s), hence capillarity (mm/hr) of water along the wick.

The distance of the fluid along the wick at regular intervals was plotted against time to obtain an empirical relationship that represents the temporal rise of the working fluid for the PE wick (Fig. 13b), which was,

$$\text{height of fluid along the wick} = 15.834\ln(\text{time}) + 5.308.$$

The capillarity of the wick was found to be approximately 135mm/hr. Table 3 below contains a summary of the wick properties.

Table 3: Wick properties

<b>Material</b>	Polyethylene
<b>Nature</b>	Hydrophilic
<b>Physical appearance</b>	White, section in contact with the evaporator impregnated with <1% v/v Cu nanoparticles of 30nm particle size.
<b>Thickness [mm (inches)]</b>	0.6 (0.024)
<b>Area on evaporator</b>	80mm x 160mm
<b>Porosity</b>	34%
<b>Permeability (m<sup>2</sup>)</b>	1.67x10 <sup>-11</sup>
<b>Capillarity (mm/hr)</b>	~135
<b>Average pore size (Microns)</b>	95
<b>Wicking volumetric flowrate (mm<sup>3</sup>/s)</b>	18.1
<b>Average wicking velocity (mm/s)</b>	0.554

### 3.1.3 Procedure for comparing the integrated wick with a plain PE wick and other conventional evaporative cooling apparatus

The experiment was first carried out with heat pipes – in still air and fan-assisted conditions. A picture of the setup is shown in Fig. 14, where the red-bordered yellow dots show some of the thermocouple locations. In addition, two thermocouples are sandwiched between the heat block and the TEGs to monitor the ‘hot side’ temperature, and two other thermocouples sandwiched between the heat pipes and the other side of the TEGs to monitor the ‘cold side’ temperature.

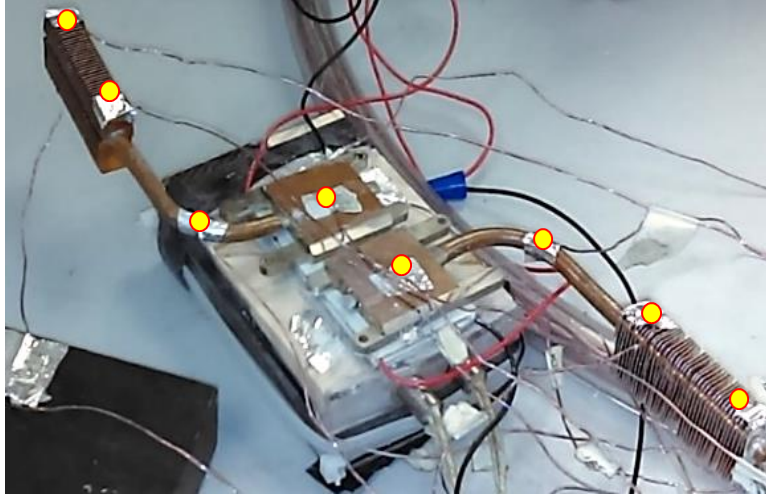


Figure 14: Picture of the setup with heat pipes. The TEGs are sandwiched between the heat pipes and the heat cartridge/block, together with thermocouples on both sides of the TEGs. The yellow dots show other thermocouple positions.

For the fan-assisted heat pipe experiment, a 120V, 0.57A Aerospeed fan (model BX100) is used. It is set to low revolution speed and positioned approximately 8ft away from the setup. The resulting wind speed, measured with an Omega HHF 1000 series anemometer, was 0.7m/s.

To replicate a loop heat pipe setup, emphasis was placed on the evaporator and the compensation chamber sections since they are key to the proof of concept experiments. Hence, as evaporation occurred, the compensation chamber was manually topped up where applicable, as in Fig. 15 setup for the experiment with the metal wick. A compact channel is used with the metal wick to aid with vapor escape as the setup orientation is pro-gravity.

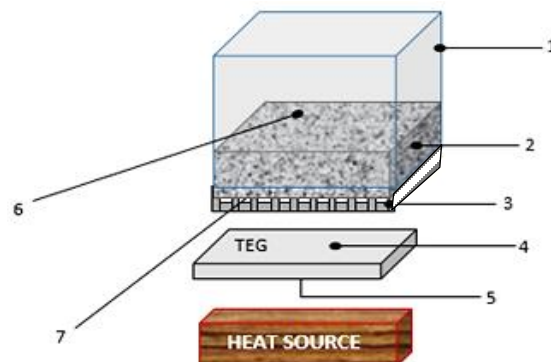


Figure 15: Picture and schematic of the setup with metal wick. (1) Compensation chamber (2) Saturated metal wick (3) Compact channel (4) – (7) Thermocouple positions.

The nanoparticle used for this test is the 20nm, hydrophilic Alumina ( $\text{Al}_2\text{O}_3$ ). 1.5g of this nanoparticle was thoroughly mixed with 12 ml of Dimethylacetamide (DMAc), which corresponds to approximately 3.14% volume fraction, under a fume hood. The suspension was thereafter applied/poured on the roughened sections of the wick and subjected to an oven temperature of  $60^\circ\text{C}$  for 15 hours, placed horizontally on a glass sheet. The result was well-dispersed and strongly bound  $\text{Al}_2\text{O}_3$  nanoparticles on both roughened surfaces of the wick. Fig. 16 shows the setup for experiments with the wick.

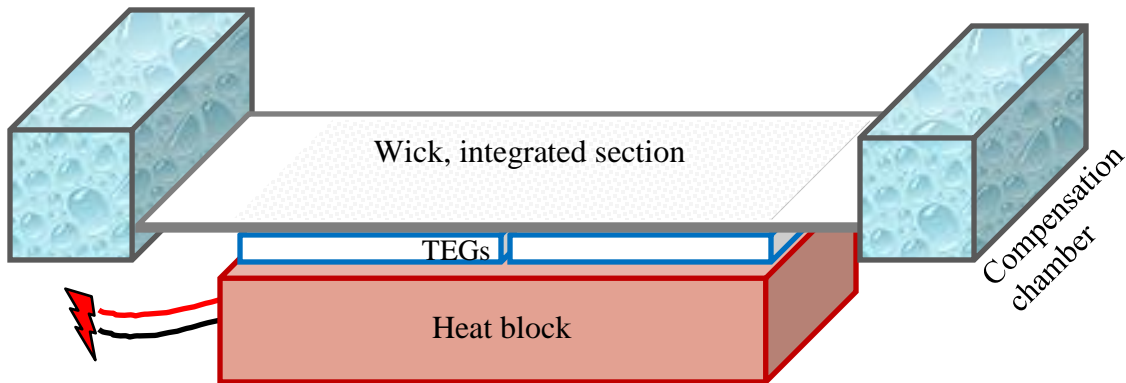


Figure 16: Setup schematic of tests with the PE wick. Thermocouples are sandwiched between the TEGs and the wick, and between the TEGs and the heat source.

The integrated and plain PE wick, respectively, are replenished with working fluid from the reservoir/compensation chamber. The thermoelectric modules are sandwiched between the wick, representing the heat sink, and the heat block, which is the heat source. The experiments were carried out at an ambient temperature of  $23.8^\circ\text{C}$  ( $74.84^\circ\text{F}$ ) and  $0\text{m/s}$  as recorded by a digital thermometer and the aforementioned anemometer, respectively, besides the second heat pipe experiment that had an imposed ambient air velocity of  $0.7\text{m/s}$ .

The thermocouples used are T-type Copper-Constantine, connected to an Agilent 34970A Data Acquisition/Switch Unit to automatically monitor the temperature variations in the course of the experiment. Thermal grease of  $2.308\text{ W/mK}$  is thinly applied over the surface of the rubber heaters and the TEGs to eliminate air gaps between the heaters, the TEGs and the heat sinks in use. The approximate thickness of the thermal grease over the surfaces of the heaters and the TEGs is  $1.5 \times 10^{-4}\text{ m}$ . Silver epoxy of approximately  $2\text{ W/mK}$  was used to hold thermocouples in place on

top of the TEG to measure the temperature of the TEG surface in contact with the heat sink. The heating power was varied from 0.53 W/cm<sup>2</sup> to 1.62 W/cm<sup>2</sup> with a variable autotransformer, as shown in Table 4. The temperature and voltage generated by the TEGs throughout the experiments were automatically recorded by the data acquisition unit.

Table 4: Heat loads used in the experiment (the power input values in asterisks were only tested for heat sinks that were able to keep the TEG hot side temperature below 160°C on a 1.62W/cm<sup>2</sup> power input).

<i>Voltage from the variable autotransformer (V)</i>	<i>Equivalent Watts (W)</i>	<i>Equivalent Heat Flux (W/cm<sup>2</sup>)</i>
0	3.33	0.10
20	16.46	0.53
25	25.72	0.83
30	37.04	1.19
35	50.40	1.62
40*	66.25*	2.12*

### 3.1.4 Procedure for tests on nanoparticle percent fraction for immobilization and the effect of wick thickness

The immobilization procedure with Al<sub>2</sub>O<sub>3</sub> for tests to determine a suitable nanoparticle percent fraction for immobilization is similar to that described in the previous section. Thermal grease of 2.308W/mK is thinly applied over the surface of the four silicone rubber heaters to eliminate air gaps between the heaters and the TEG. The approximate thickness of the thermal grease over the surface of the silicone rubber heaters is 1.5x10<sup>-4</sup>m. Micro grooves are made on both sides of the wick to allow for thermocouple insertion without creating an air gap. This did not make the arrangement perfectly air tight but enabled a very good approximation. The thermocouples used are T-type Copper-Constantine, connected to an Agilent 34970A Data Acquisition/Switch Unit to automatically monitor the temperature variations in the course of the experiment. Power into the silicone rubber heaters using a variable DC regulated power supply is outlined in Table 5.

As the power is varied, the temperature on both sides of the wick is monitored via the thermocouples and each power input is left long enough to attain steady state. Each experiment lasted at least 300 scans of 30 secs each, corresponding to at least 150 minutes. This was observed to be within a time range for irrefutable transition to steady state based on observation from earlier experiments. The voltage was observed using the data acquisition unit by connecting the TEG wires directly, so as to record its temporal evolution during the experiment.

Table 5: Power supplied to the heaters for the experiment

Watts (W)	Equivalent Heat Flux ( $\text{W}/\text{cm}^2$ ) ( $\pm 4\%$ )
<b>1.526</b> (21.8V x 0.07A)	<b>0.1</b>
<b>4.047</b> (35.5V x 0.114A)	<b>0.25</b>
<b>8.974</b> (53.1V x 0.169A)	<b>0.56</b>

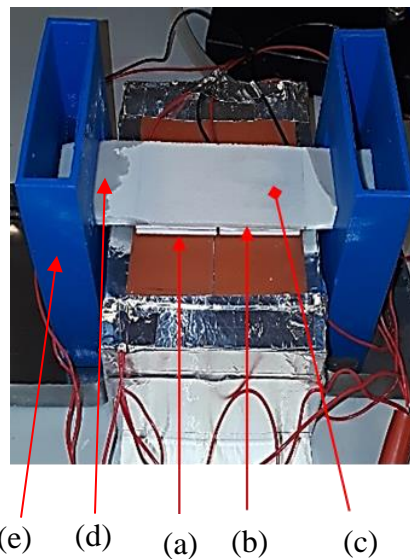


Figure 17: Setup for nanoparticle percent fraction and thickness tests. (a) Heat source; (b) Heat sink side; (c) Top of the wick; (d) working fluid (water) as it wicks across; (e) compensation chamber.

For tests on wick thickness, Cu nanoparticles were used to gauge the power production enhancement, using the best performing wt./wt. nanoparticle concentration as determined from the previous experiment. This test is done for different wick thickness: 0.024”, 0.062”, 0.125” and 0.250” and juxtaposed with their plain wick counterparts to observe the contribution of the immobilized nanoparticle to thermoelectric power generation as the wick thickness increased.

In preparing the nanoparticle suspension for immobilization on the PE wick substrate, sonication was found to have negligible effect on the Cu nanoparticles, unlike Alumina. Vigorously shaking the Cu nanoparticles in DI water led to a much more uniform suspension for the immobilization process on the wick, which was the process adopted for this test.

### 3.2 Main Setup Process Flow Schematic and Design

The fundamental principle is shown in Fig. 18. Ambient heat/waste heat is incident on the evaporator, which transfers the heat energy to the top side of the TEGs. The bottom side is cooled with the custom heat sink so as to obtain the temperature differential necessary for power production via the Seebeck effect.

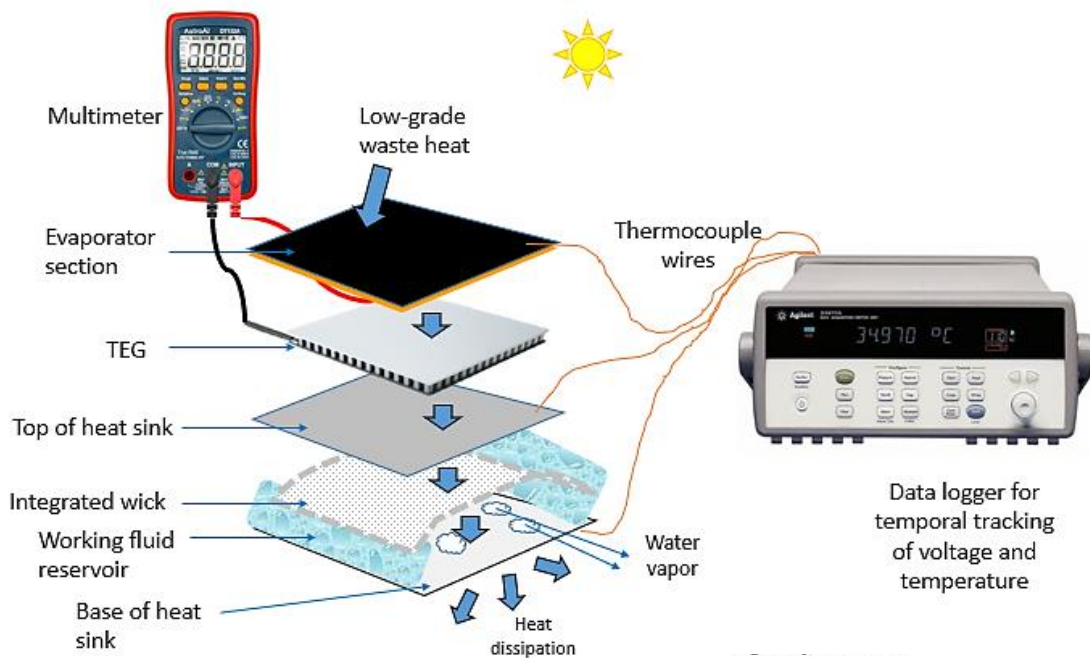


Figure 18: Process flow schematic

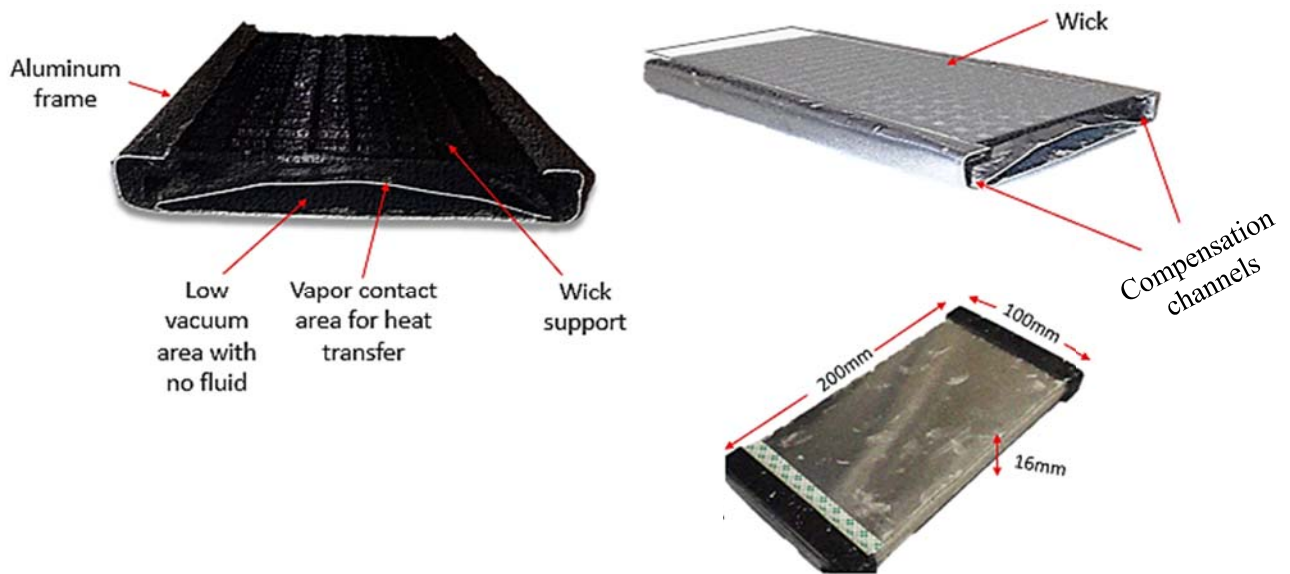


Figure 19: Heat sink design

The wick support is a plastic support with regularly spaced openings, necessitated by the orientation of the wick in the heat sink as anti-gravity (evaporator-above-condenser) since the PE wick is not rigid and cannot sustain itself in such position. Furthermore, a direct correlation between strong contact between the wick and the TEGs and enhanced performance have been observed in previous experiments and the wick support will also enable such contact.



Figure 20: Wick support, top view. The openings allow for downward vapor displacement to the Aluminum wall of the heat sink, without compromising the structural integrity of the support in maintaining uniform contact between the wick and the TEGs.

### 3.3 Design Calculations

#### 3.3.1 Heat Sink Pressure

The working fluid is deionized water and the desired boiling temperature of working fluid = 45°C (318K).

Rearranging the Clausius-Clapeyron equation, we have:

$$P_2 = P_1 e^{\left(\frac{-\Delta H_{\text{vap}}}{R} \left[\frac{1}{T_2} - \frac{1}{T_1}\right]\right)} \quad (15)$$

Where,

$T_2$  = the boiling point at the pressure of interest, = 318 K

$R$  = the ideal gas constant,  $8.314 \text{ J} \cdot \text{K}^{-1} \cdot \text{mol}^{-1}$

$P_2$  = the vapor pressure of the liquid at the pressure of interest

$P_1$  = the pressure where the corresponding  $T_1$  is known, (101.32 KPa )

$\Delta H_{\text{vap}}$  = the heat of vaporization of the liquid at  $P_1 = 40660 \text{ J} \cdot \text{mol}^{-1}$  ( $\equiv 2257 \text{ J/g}$ )

$T_1$  = the boiling temperature at  $P_1$  (373.15 K)

Solving the equation,  $P_2$  is found to be  $\approx 10 \text{ KPa}$  (0.1 bar) for the vapor pressure of the fluid to equal its surrounding pressure at  $\approx 45^\circ\text{C}$ .

#### 3.3.2 Fluid Volume and Rate of Evaporation

The area of the heat source surface of the device is  $0.0128 \text{ m}^2$  (80 mm x 160 mm). Assuming a sun power of  $1000 \text{ W/m}^2$ , the anticipated incident power on that area is approximately 13 Joules every second. To ensure enough working fluid, the power to be used for analysis is taken as  $15 \text{ J/s} \equiv 15 \text{ W}$ .

$$\text{Mass evaporated per second basis, } \dot{m} = \frac{Q}{h_{\text{fg}}} = \frac{15 \text{ J/s}}{2392940 \text{ J/kg}} = 6.27 \times 10^{-6} \text{ kg/s.}$$

$$\text{Equivalent volume of water evaporated} = \frac{\dot{m}}{\rho} = \frac{6.27 \times 10^{-6} \text{ kg/s}}{990 \text{ kg/m}^3} = 6.33 \times 10^{-9} \text{ m}^3/\text{s} \text{ or } 0.00633 \text{ ml/s, or } 6.33 \text{ mm}^3/\text{s.}$$

Volume contained by wick under evaporator area =  $2611.57 \text{ mm}^3$  or 2.61ml (volume of wick area in contact with the TEGs multiplied by the porosity of the wick).

$\frac{2.61 \text{ ml}}{0.00633 \text{ ml/s}} \approx 6.9$  minutes to evaporate all the water in the wick.

Hence, the fluid volume in the compensation chamber is chosen to be  $6.9 \times 2.61 \text{ ml} \approx 18 \text{ ml}$ , to ensure dry out never occurs.

Let the longest distance for fluid in the wick to travel be denoted as  $d$ , and equal to 85mm (Fig. 21). From the empirical relation obtained from Fig. 13b:

$$d = 15.834 \ln(t) + 5.308, \quad (16)$$

where  $t$  is time. Hence, time ( $t$ ) for 85mm = 153.4s. From this, velocity =  $5.54 \times 10^{-4} \text{ m/s}$ .

[Area of wick in direction of flow] x [porosity] = actual flow area, and this gives  $3.264 \times 10^{-5} \text{ m}^2$ . Multiplying this by the velocity gives the volumetric flowrate as  $1.81 \times 10^{-8} \text{ m}^3/\text{s}$  or  $18.1 \text{ mm}^3/\text{s}$ . This is almost three times the evaporation rate per second, thus the wick can handle the evaporation.

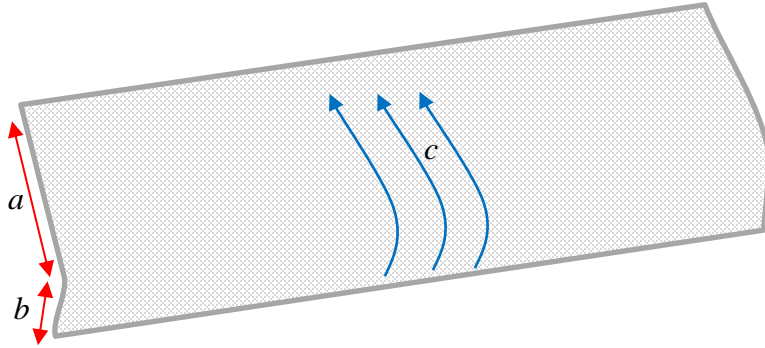


Figure 21: Dominating flow pattern from compensation channel across the wick.  $a$  = width of wick area under the TEGs (80 mm);  $b$  = length of wick in compensation channel (10 mm);  $c$  = dominating flow direction. The channel fluid height is approximately 5 mm.

### 3.3.3 Wick Boiling Limit

The boiling limit is given by,

$$q_b = \frac{\lambda_w \Delta T_s}{x}, \quad (17)$$

where

$$\Delta T_s = \frac{\Delta P \cdot T_{\text{sat}} (v_v - v_l)}{h_{fg}} \quad (18)$$

$\Delta P = 10$  KPa and  $x$  is the thickness of the wick structure. Through the experiment described in Section 3.1.2.2, the effective conductivity of the wick,  $\lambda_w$ , is calculated to be  $0.661$  W/m°C.

$\Delta T_s$  is found to be  $\approx 2.82^\circ\text{C}$ . With  $x \approx 0.0006\text{m}$ , the  $Q_{\text{limit}}$  is found to be  $\approx 39.8$  W. This is more than the projected power of  $15$  W, so there is no risk of boiling limit challenges. Fig. 22 shows a comparison of the calculated values of the boiling limit without the integration of nanoparticles or with a higher  $x$  value of the wick. It shows the first proof on why an integrated wick of  $\sim 0.6\text{mm}$  is a good choice.

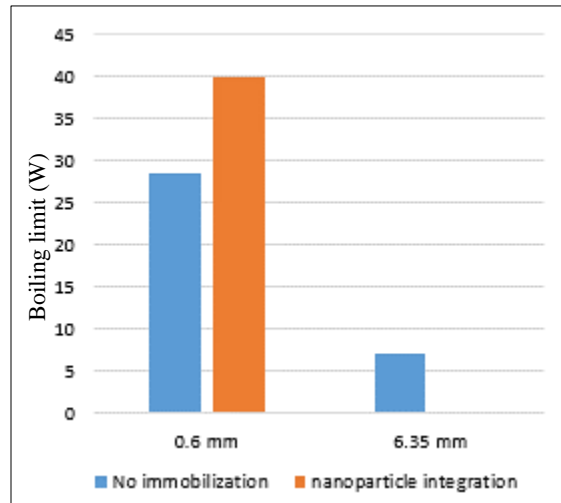


Figure 22: Calculated boiling limit comparisons

### 3.3.4 Pressure Drop and Permeability

From Darcy's law for transport in porous media,

$$Q = \frac{K \cdot \Delta P \cdot A}{\eta \cdot \Delta L}, \quad (19)$$

$Q$  = flow rate ( $\text{m}^3/\text{s}$ )

$K$  = permeability coefficient ( $\text{m}^2$ )

$\Delta P$  = pressure drop or difference (Pa)

$\Delta L$  = flow length or thickness of test sample (m)

$A$  = area of cross-sectional area to flow ( $\text{m}^2$ )

$\eta$  = fluid viscosity (Pa.s)

But,

$$\Delta P = \frac{\Delta F}{A} = \frac{m \cdot \Delta a}{A}, \quad (20)$$

Where  $m$  is mass of the fluid and  $A$  is the area of the wick in direction of flow. To obtain the change in acceleration of flow,  $\Delta a$ , equation (16) -- the empirical distance-time relationship of working fluid in the wick -- is differentiated twice and the resulting rate of change of velocity is obtained:  $15.834 \text{ m/s}^2$ .

$$\text{Hence, } \Delta P = \frac{m \cdot \Delta a}{A} = \frac{(0.00129 \text{ Kg})(15.834 \text{ m/s}^2)}{3.264 \times 10^{-5} \text{ m}^2} \approx 626 \text{ Pa.}$$

Making  $K$  the subject of equation (19), with  $\Delta P = 626 \text{ Pa}$ ,  $A = 9.6 \times 10^{-5} \text{ m}^2$ ,  $Q = 1.81 \times 10^{-8} \text{ m}^3/\text{s}$ ,  $\Delta L = 0.085 \text{ m}$ , and  $\eta = 0.000653 \text{ Pa}\cdot\text{s}$ , the permeability of the wick is obtained as  $1.67 \times 10^{-11} \text{ m}^2$  or  $1.67 \times 10^{-7} \text{ cm}^2$ .

Thus, the pressure drop is negligible, and the permeability is comparable to conventional wicks in heat pipes [115].

### 3.3.5 Heat Transfer from the Heat Sink to the Ambient

The premise for this calculation is that the flow is external, the boundary layer is laminar and the fluid properties are assumed constant.

The heat sink is considered a rectangular cylinder with rounded corners in cross flow instead of a flat plate (Fig. 23). The exposed flat side is facing downwards, thus the majority of fluid interaction will be in cross flow from the sides.

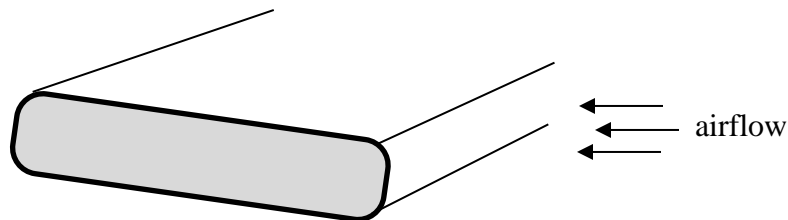


Figure 23: Heat sink geometry schematic

For this geometry,  $D$  is the length perpendicular to the direction of flow [116], = 0.016m. For an average air velocity of 1 m/s, the Eckert number ( $v^2/C_p\Delta T$ ) and Brinkman number ( $Ec.Pr$ ) are  $< 1$ , so there is negligible viscous dissipation or external heating effect due to velocity of convective current.

$T_{\infty,avg} = 25^\circ\text{C}$ ,  $T_{w,avg} = 50^\circ\text{C}$  (as observed from preliminary tests), so  $T_f = 37.5^\circ\text{C}$ . So, fluid properties for the succeeding calculations were obtained at  $T_f = 37.5^\circ\text{C}$ .

For  $Re_D.Pr \geq 0.2$ , the average  $Nu_D$  according to Churchill and Bernstein's correlation [116] is:

$$\overline{Nu}_D = 0.3 + \frac{0.62Re_D^{1/2} Pr^{1/3}}{[1 + (0.4/Pr)^{2/3}]^{1/4}} \left[ 1 + \left( \frac{Re_D}{282000} \right)^{5/8} \right]^{4/5} \quad (21)$$

Also,

$$\text{Convective heat coefficient, } h, = \frac{Nu.K}{D} \quad (22)$$

$$\text{From Newton's law of cooling, } Q = hA(T_w - T_\infty) \quad (23)$$

Using equations (21) to (23), the values in Table 6 are obtained, together further details on the heat sink design:

Table 6: Summary of heat transfer calculations on heat sink prototype

Basis: low ambient air current ( $\approx 1$ m/s)
$Nu_{avg} = 15.6$
$h_{avg} = 26.4 \text{ W/m}^2\text{K}$
$Q$ (Newton's law of cooling) $\approx 17.4 \text{ W}$
Biot number = $L_c.h/k$ (where $L_c = V_{metal}/A_{surface \text{ area}}$ ) = 0.00025
$k_{metal} \approx 180 \text{ W/mK}$ (Aluminum 3003 H14) [114]
Young's modulus: 70 GPa [114]
Metal thickness $\approx 1.7 \text{ mm}$

The Biot number is  $\ll 1$ , which shows that the heat sink can be considered thermally simple or thermally thin, so no thermal gradient develops within the wall and the wall temperature can be considered constant throughout the wall thickness.

From the calculation results on Table 6, it is evident that the expected thermal load of 15W can be effectively dissipated through the heat sink.

## CHAPTER 4. RESULTS AND DISCUSSION

### 4.1 Linearity of Voltage Increment with Number of Modules

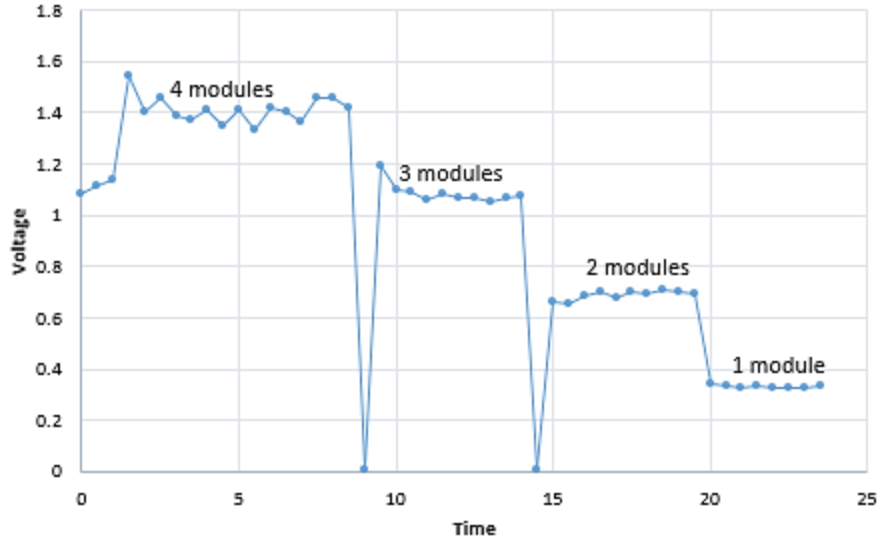


Figure 24: Change in voltage with increase in the number of thermoelectric modules.

Most of the preliminary tests were done with two thermoelectric modules, hence the question arises as to whether the results obtained can be linearly extrapolated for a greater number of modules. This result shows that the voltage obtained progresses linearly with increase in the number of thermoelectric modules, which validates the hypothesis. The sharp drops in the graph occurred when the setup is briefly disconnected so that another thermoelectric module can be added.

### 4.2 Seebeck Coefficient of the Modules

The Seebeck coefficient, a ratio of obtained voltage to temperature difference, can offer some insight on how many thermoelectric modules would be needed for this device in harvesting waste heat, considering a balance of effectiveness and portability has to be met. The number of modules to be used in harvesting waste heat with the heat sink has to be realistic enough to meet the objective; at the same time, too many modules would make the entire setup bulky/unwieldy and would require a larger heat sink.

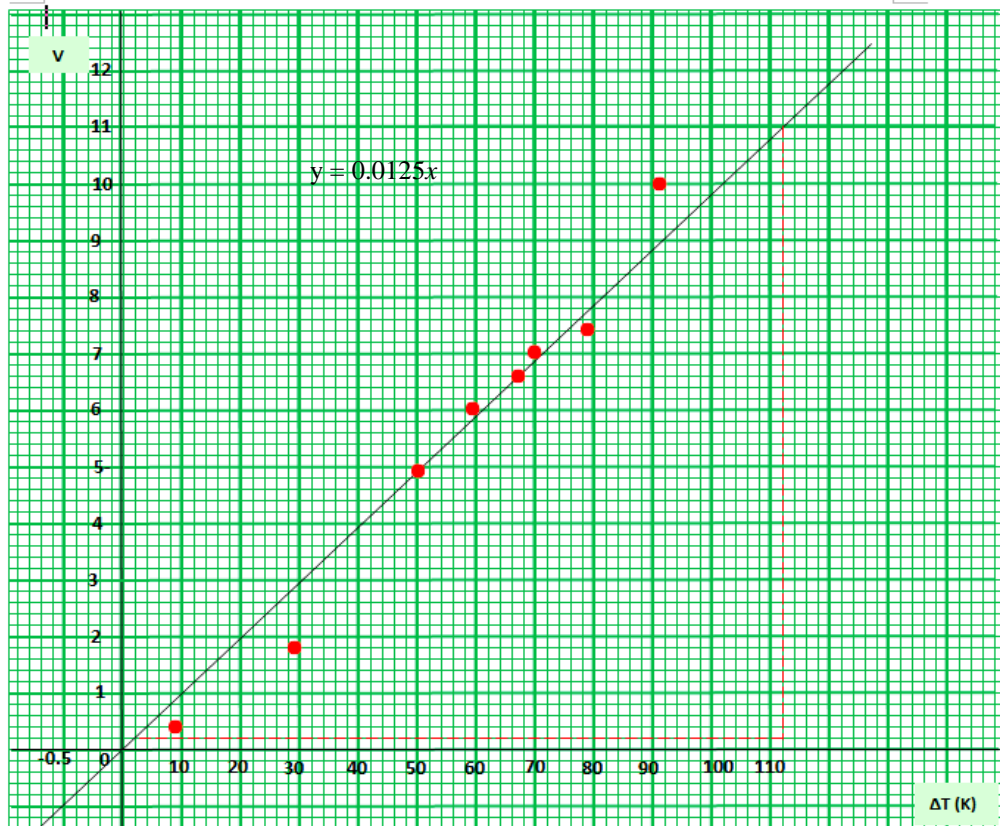


Figure 25: First experiment on increase in voltage with change in  $\Delta T$

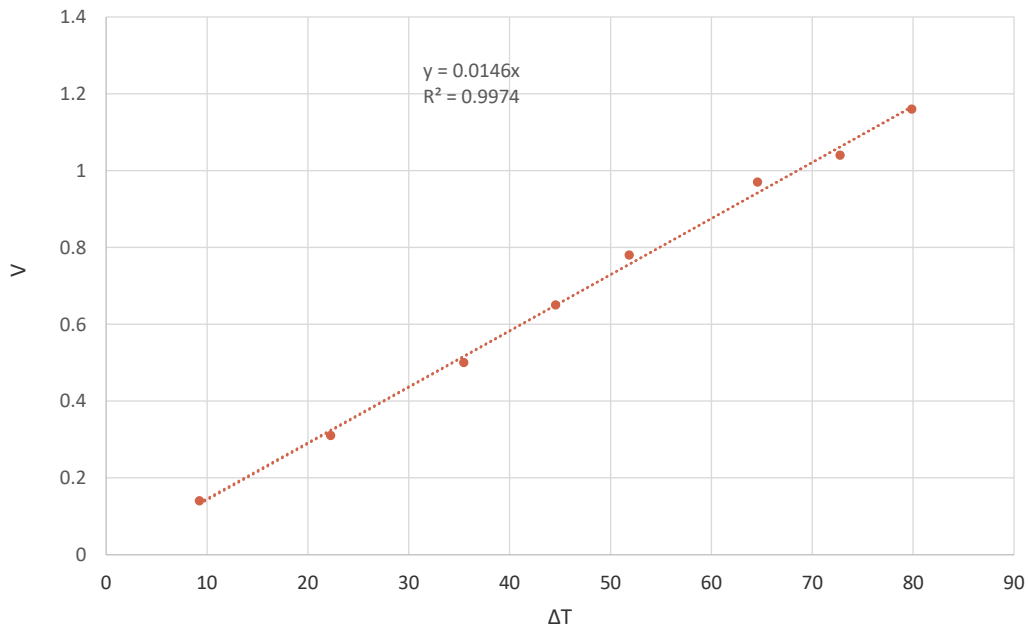


Figure 26: Second experiment on increase in voltage with change in  $\Delta T$

From these two different experiments, the Seebeck coefficients obtained were:  $\alpha = 0.0125\text{V/K}$  and  $\alpha = 0.0146\text{V/K}$ , respectively, per module. Hence, the Seebeck coefficient for the module is taken to be  $\approx 0.01\text{V/K}$ .

Going by this coefficient, that means for a heat source of  $373\text{K}$ , for example,

6 TEMs should attain  $5\text{V}$  at  $\Delta T = 83.3$

8 TEMs should attain  $5\text{V}$  at  $\Delta T = 62.5$

Considering the heat sink would be up to  $45^\circ\text{C}$ , it follows that a heat source of  $128.3^\circ\text{C}$  would be required for six TEGs to attain  $5\text{V}$ , while  $107.5^\circ\text{C}$  would be required for eight TEGs to do the same. Four TEGs will require a heat source of  $170^\circ\text{C}$  while ten TEGs will require a heat source of  $95^\circ\text{C}$ .

Since this is to operate with low grade waste/ambient heat, the higher the temperature required, the more time it would take to attain it. In many situations, low grade heat source temperatures of  $170^\circ\text{C}$  may actually be extremely difficult to attain. On the contrary, while  $95^\circ\text{C}$  heat source temperature can be easily attained and under the shortest amount of time compared to the rest, ten TEGs would make the device larger, hence less portable. Thus, on a balance of feasibility and portability, the thermoelectric generator will comprise of 8 TEGs; Fig. 27 shows the arrangement of the thermoelectric generators for the evaporator section.

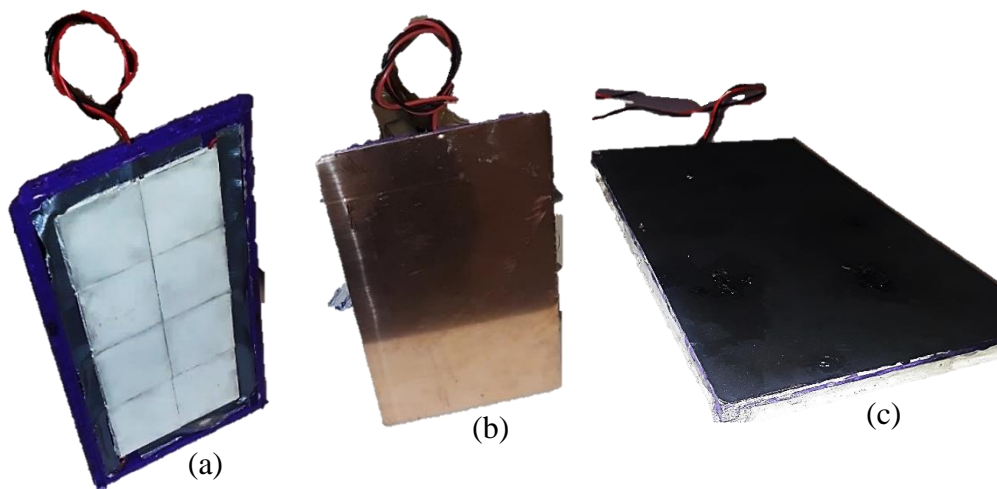
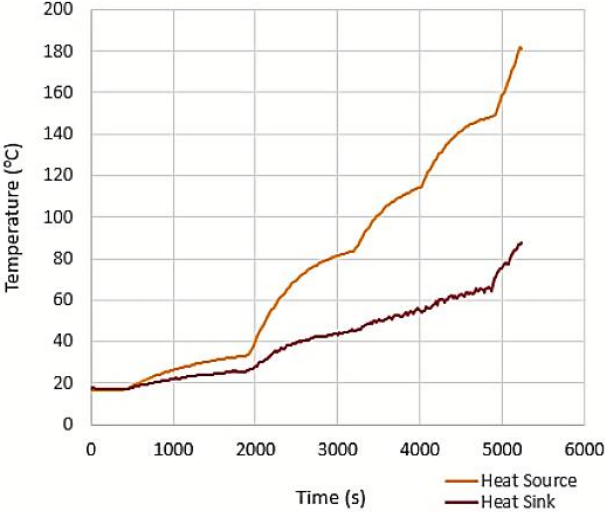
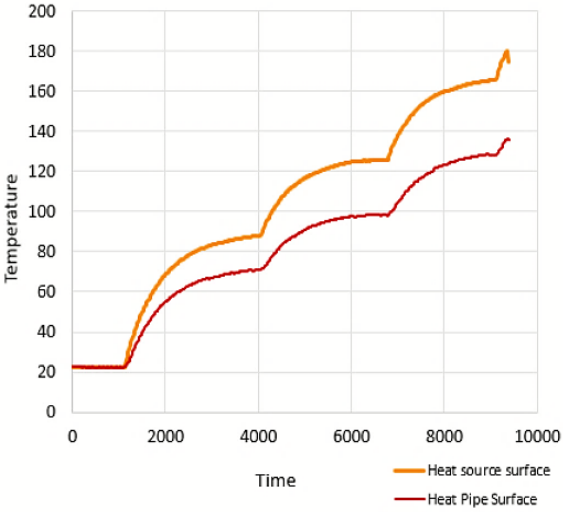


Figure 27: The TEG evaporator area. (a) Front view and (b) back view of the TEGs. (c) the metal back side is lightly coated with a black substance to enhance the absorption and retention of incident heat on the TEGs.

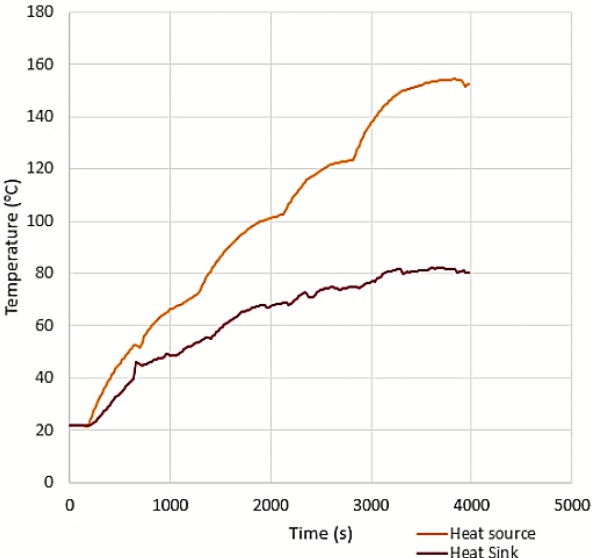
**4.3 Effectiveness of the Integrated PE Wick Compared to a Heat Pipe and Metal Wick**



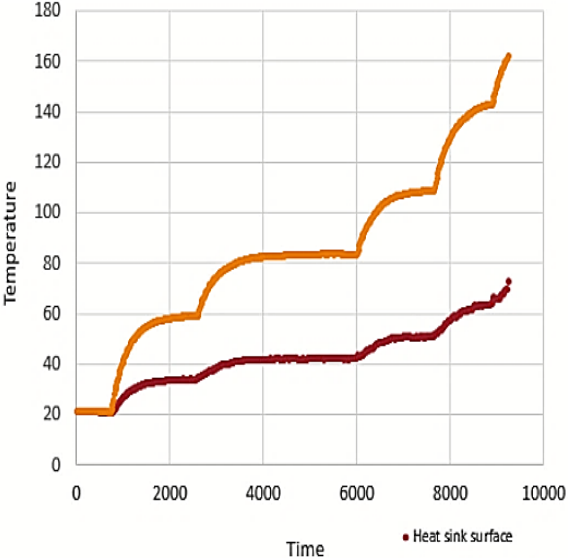
(a) Plain PE Wick



(b) Heat pipe with 0m/s wind velocity



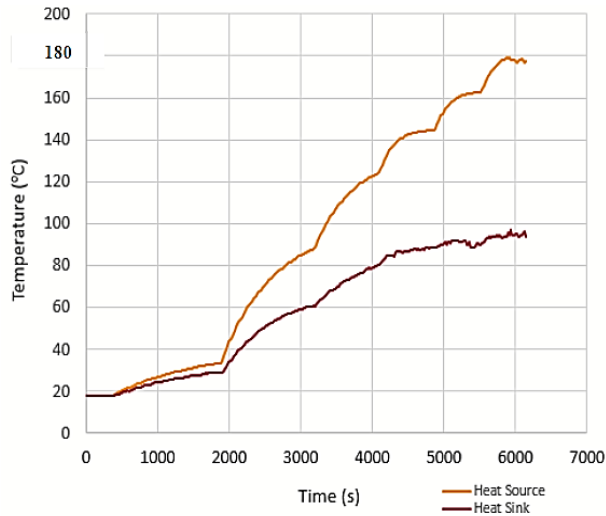
(c) Metal foam



(d) Heat pipe with gentle air flow (0.7 m/s)

Figure 28 (a-e): Variation of heat source and heat sink temperature with time.

Figure 28 continued.



(e) PE wick integrated with nanoparticles

For thermoelectric generators, it is established that there is a direct correlation between an obtained temperature difference and the voltage. Hence, setups with better thermal management recorded a higher temperature difference and higher voltage. The incident thermal energy on one side of the TEG is conducted to the other side where the heat sink facilitates a transfer of the energy to the ambient. The more effective this heat sink, the more effective the TEG and the higher the voltage obtained.

The metal foam (Fig. 28c) and the PE wick without immobilized nanoparticles (Fig. 28a) had better performance compared to the Heat Pipe with 0 m/s wind speed ambient condition (Fig. 28b). However, thermal leak to the reservoir of the metal wick and the poor thermal conductivity of the PE wick did affect the thermal management efficacy of both setups. This agrees well with literature as the adverse effect of thermal leak with metal wicks have been widely reported, together with the uneven thermal distribution in non-metal wicks.

The PE wick integrated with nanoparticles and the fan-assisted heat pipe had the best performance and even exceeded 5V, due to their superior thermal management. The weakest performance was recorded by the heap pipe at 0m/s wind velocity, thus revealing the significance of convective currents around the condenser section of heat pipes.

Nanofluids are reported to have better thermal conductivity than ordinary heat sink fluids [30, 31]. This thermal conductivity enhancement has been attributed to the Brownian motion of the nanoparticles within the fluid and increase in thermal conductivity due to the suspension of nanoparticles [32, 33]. This implies that immobilized nanoparticles would not be as efficient as nanofluids due to the lack of Brownian motion activity, but by virtue of the nano-metals being suspended within the wick, the overall conductance of the wick-fluid system will be enhanced as the working fluid flows through the non-metal wick. This phenomenon is suspected to have led to the enhanced performance of the nanoparticle-assisted PE wick.

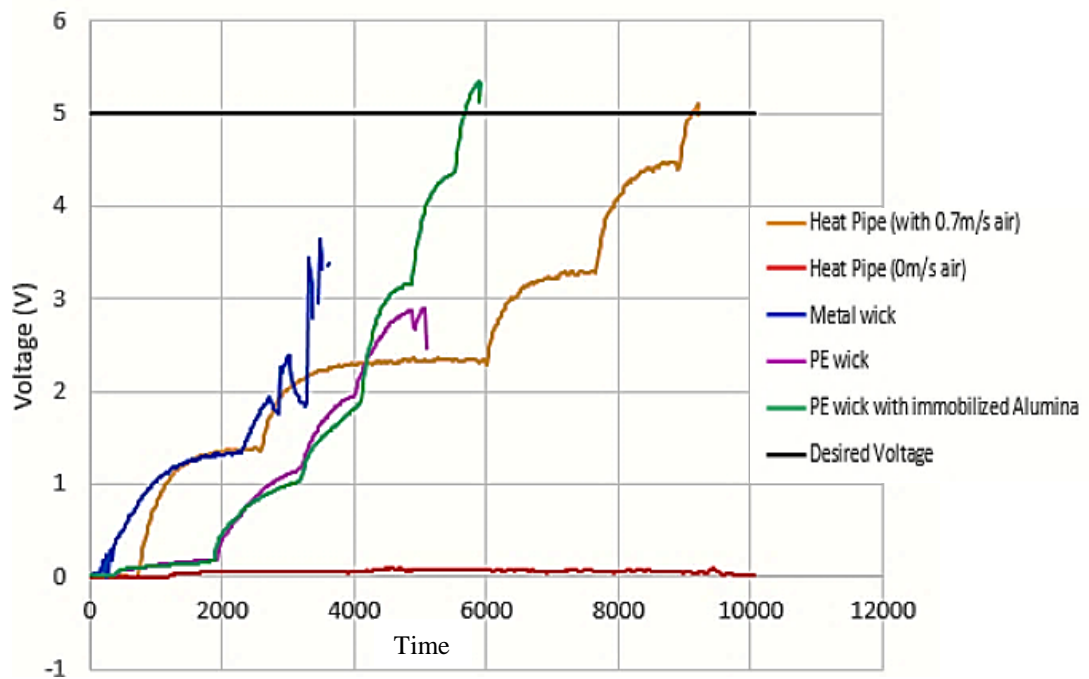


Figure 29: Voltage comparison for the different experiments.

Due to the superior thermal management of the integrated wick, at  $1.62 \text{ W/cm}^2$  the temperature of its hot source area was less than  $140^\circ\text{C}$ , compared to over  $180^\circ\text{C}$  for the plain PE wick. This enabled the integrated wick to take on a higher power density of  $2.12 \text{ W/cm}^2$  (tests were terminated for any TEG with over  $180^\circ\text{C}$  heat source temperature). So, despite having an approximately equal temperature difference (Fig. 28a, e), a comparison of the obtained voltage (Fig. 29) for the plain PE wick and the PE wick integrated with Alumina nanoparticles suggests that more exergy from the higher power density led to the superior performance of the integrated wick. This implies that

the quality of incident heat energy is a factor in power production via the Seebeck effect; temperature difference in isolation is not a holistic indicator. For example, a certain temperature difference between two cold temperatures will not lead to the same voltage production for the same temperature difference for a higher incident thermal energy.

Fig. 29 shows that the integrated wick, in closed room conditions (0 m/s air flow), has a comparable performance to the heat pipe in ambient conditions (0.7 m/s air flow). Nanoparticles are considered an effective solution to the thermal barrier posed by macro-scale thermal conductor contacts, as affirmed by Nnanna et al. [30]. Experimental results suggest that this thermal barrier within the PE wick-water system was indeed lessened by virtue of the immobilized alumina nanoparticles.

#### 4.4 Thermal Leakage to the Reservoir/Compensation Channels

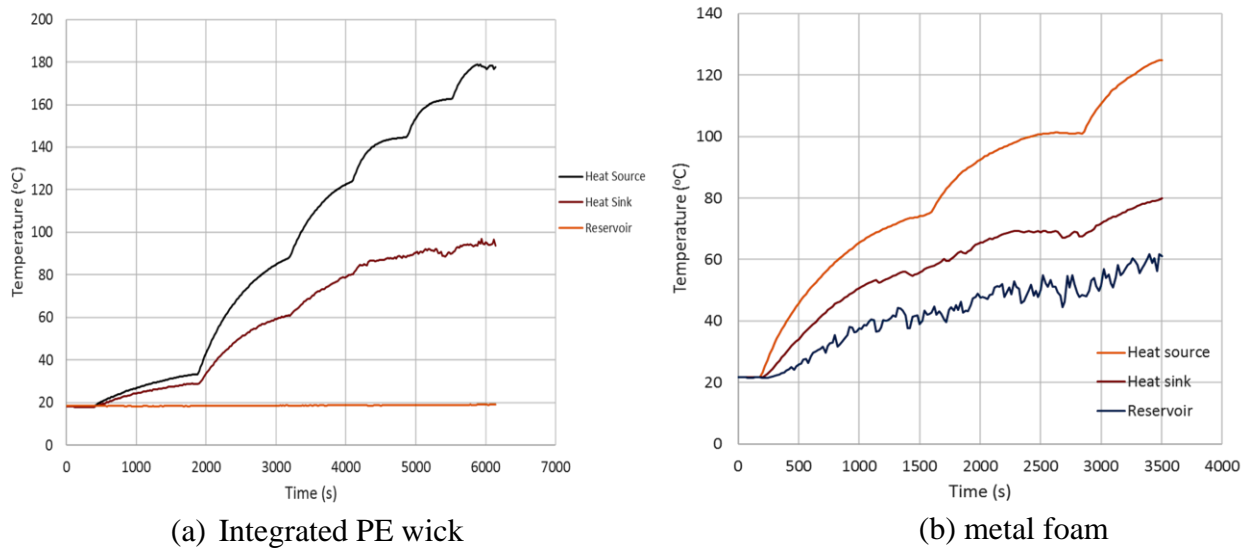


Figure 30: Temporal evolution of temperature in reservoir/compensation channels

Fig. 30 highlights the thermal leak challenge of metal wicks. By contrast, the integrated PE wick recorded negligible temperature change in its compensation channels. This underscores the viability of immobilizing nanoparticles on an area of interest to enhance the radial thermal

conductance of the zone yet prevent axial thermal conductance back to the compensation channel or reservoir – the bane of metal wicks.

#### 4.5 Attrition of Immobilized Nanoparticles on the Wick

The wicks were weighed before and after immobilization and after the experiments, to observe the weights of the PE wick so as to check if the nanoparticles were being eroded during the experiments as the water wicked through the substrate. The relationship between the vol/vol% Alumina suspension in the DI water solvent and the wt/wt % of Alumina/wick is shown in Fig. 31.

Table 7: Determination of immobilization wt/wt and check for erosion of immobilized particles.

Dry PE Wick	1% vol/vol	2% vol/vol	4% vol/vol	9% vol/vol
Pre-immobilization weight (g)	6.07	5.90	5.78	5.81
Post-immobilization weight (g)	6.34	6.51	8.09	9.67
Percent Alumina (g)/PE wick (g) <i>before</i> experiment (%)	4.45%	10.34%	39.97%	66.44%
Wick weight after experiment (g)	6.32	6.49	8.08	9.65
Percent Alumina (g)/PE wick (g) <i>after</i> experiment	4.12%	10%	39.79%	66.09%

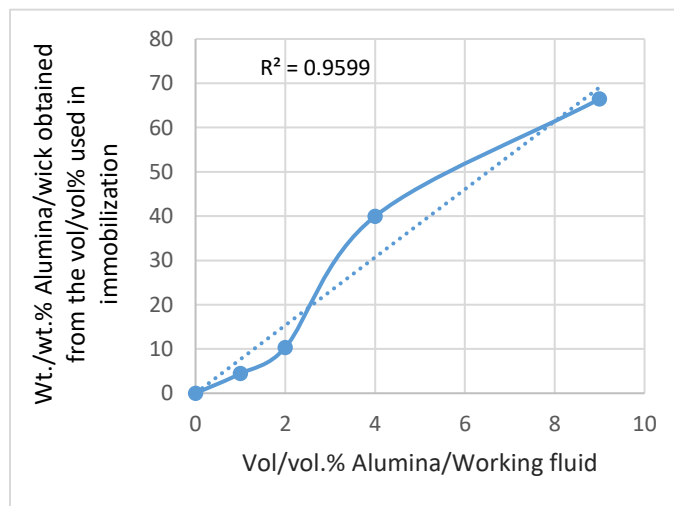


Figure 31: Relationship between the vol/vol % of alumina suspension in working fluid and the final wt/wt % of Alumina immobilization on the PE wick.

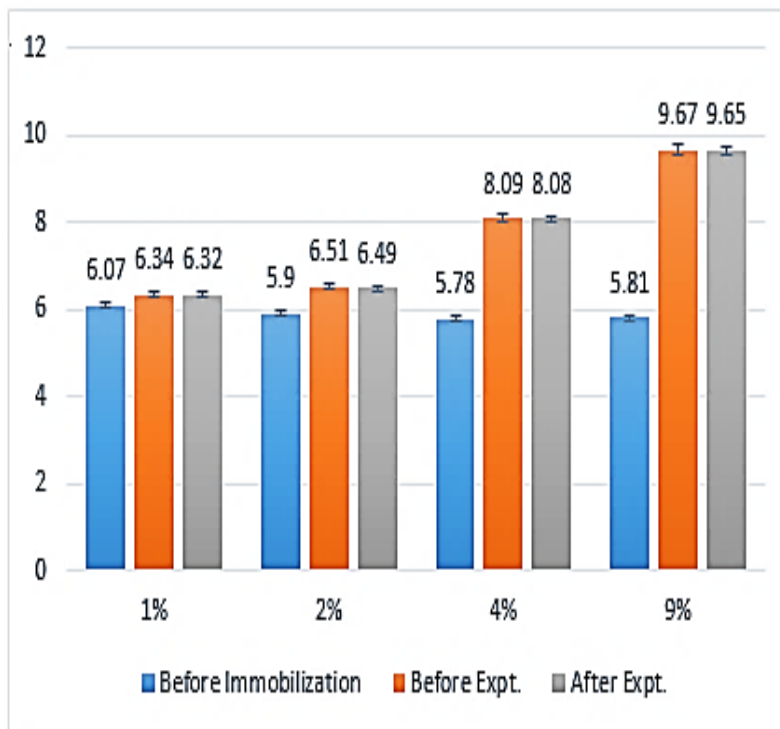
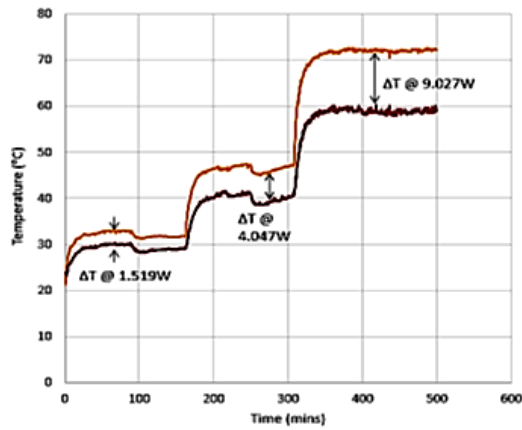


Figure 32: Bar chart showing negligible erosion of immobilized nanoparticles ( $\pm 1\%$ ).

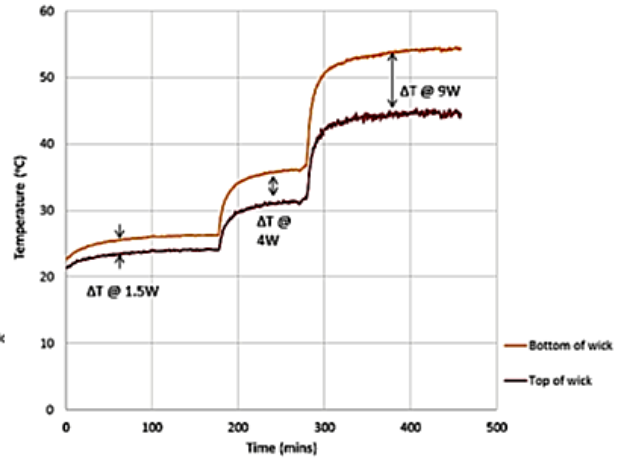
Table 7 and Fig. 32 show that the nanoparticles are strongly bound to the wicks. The weight of the wicks before and after the experiments all show a percentage difference of less than 0.4%, which is negligible. However, this is just for the observed period and over prolonged usage the cumulative erosion may become significant, although this might take a very long time judging by the minute amount being eroded, if that were to be the case.

Figure 31 shows an approximately linear relationship for the vol/vol% immobilization prepared and the wt./wt.% of Alumina-PE wick obtained. However, the plot reveals a steeper slope per increase in vol./vol% of the immobilized Alumina after 2% vol/vol of Alumina/Solvent. This suggests that more pore spaces are being taken up by the nanoparticles, which would affect the permeability of the wick. It is expected that the potential increase in conductance due to these nanoparticles would eventually become unable to negate the adverse effects of reduced permeability and altered porosity/pore characteristics of the wick.

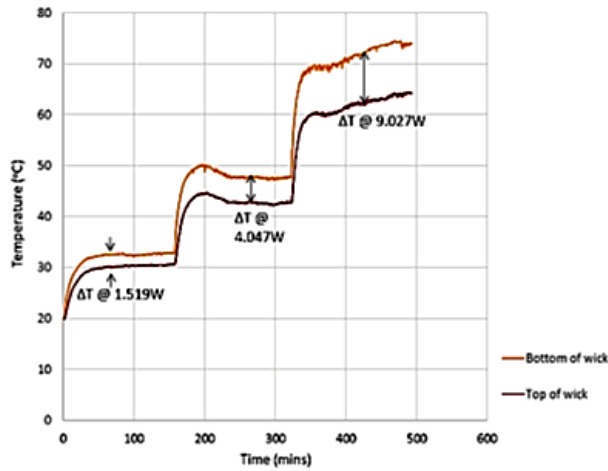
## 4.6 Nanoparticle Percent Fraction for Immobilization



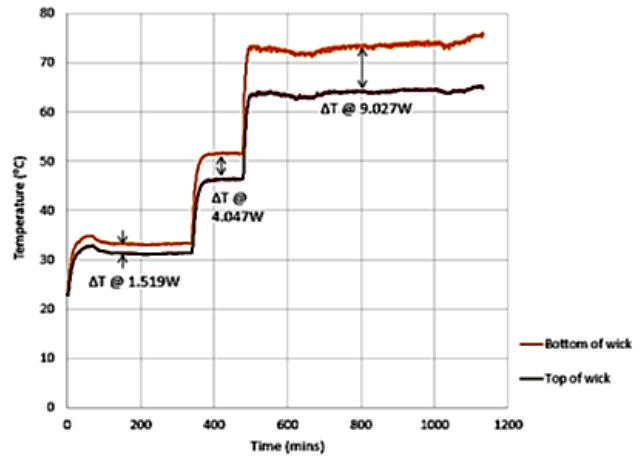
(a) Base case (no immobilization)



(b) 4% wt./wt. of nanopowder/Wick



(c) 10% wt./wt. of nanopowder/Wick



(d) 66% wt./wt. of nanopowder/Wick

Figure 33: Conductance of the wick under different nanoparticle immobilization percentages

Using the ~4%, ~10% and ~66% wt/wt nanoparticle/PE-wick, it was observed that the conductance of the wicks was boosted compared to the base case/plain PE wick (Fig. 33a). Since all experiments were carried out under exactly the same conditions, it follows that only the immobilized

nanoparticles could have resulted in the increase in conductance for the integrated wicks (Fig. 33b-d).

Table 8: Conductance results

Wt/wt.% Conc.	Power (W)	Equivalent Heat flux (W/cm <sup>2</sup> )	$\Delta T$	$R_{TH}$ (K/W)	$R_{TH}^{-1} = UA$
0 (Base case)	1.5	0.1	2.8	1.87	0.53
	4.0	0.25	6.7	1.68	0.60
	9.0	0.56	13.3	1.48	0.68
4	1.5	0.1	2.2	1.47	0.68
	4.0	0.25	4.7	1.18	0.85
	9.0	0.56	9.4	1.04	0.96
10	1.5	0.1	2.1	1.40	0.71
	4.0	0.25	5.0	1.25	0.80
	9.0	0.56	10.2	1.13	0.88
66	1.5	0.1	1.9	1.23	0.81
	4.0	0.25	5.3	1.33	0.75
	9.0	0.56	9.3	1.03	0.97

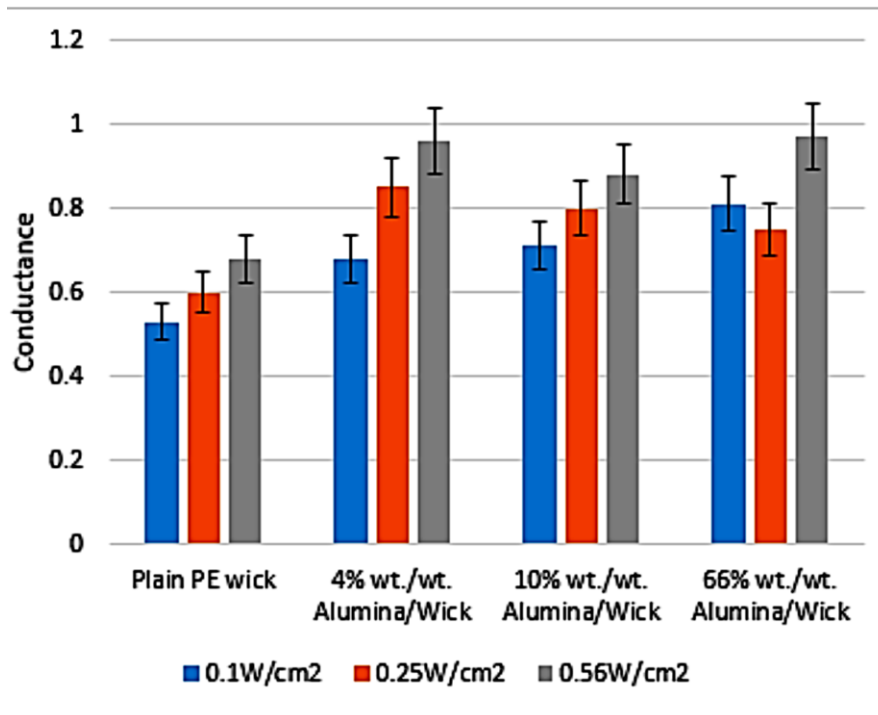


Figure 34: Comparison of the conductance of the wicks with the base case ( $\pm 8\%$ )

Thermal resistance of the wick,  $R_{TH}$  is given by  $\Delta T/W$ , where  $\Delta T$  is the temperature difference between both surfaces and  $W$  is the supplied power that induced the temperature on heat source side of the setup. The inverse of this resistance yields the conductance of the wick.

The term conductance is preferred instead of conductivity as the wick is a system of polyethylene and water, not a single solid material. One may imagine the path of energy transfer as through a system of water molecules and polyethylene walls in series, when the wick is in operation. When nanoparticles are immobilized on the wick, they attach themselves to the walls of the PE wick. These enhance the thermal response of the wick due to their inherent good thermal conductivity as the working fluid flows through the PE wick. Hence, the nanoparticles act as nano-enhancers of thermal energy transport from one PE wall or water molecule to the next.

The results on Table 8 and Fig. 34 imply that after 1% vol/vol% immobilization, resulting in 4% wt./wt. of Alumina/Wick, there is negligible enhancement in conductance. Within the limits of an 8% experimental error, the conductance due to 2% (10% wt./wt.) and 9% (66% wt./wt.) show negligible improvement over the former, even though all three are better than the base case. The anomaly on 66% wt./wt. for  $0.25 \text{ W/cm}^2$  is attributed to experimental error, being within range.

This result suggests that 4% wt/wt Alumina/PE wick could be the percentage around which an optimum balance between heat transfer and mean free path for fluid transport, including vapor escape, is more closely approximated.

After the 1% vol/vol immobilization, the performance of 2% is less, maybe due to more crowding of the nanoparticles. If these nanoparticles are imagined as nano-fins, then more crowding could interfere with the convection process as the water wicks by. Also, if some of the wick pores are compromised due to the crowding effect, it would affect thermal transport radially.

As the nanoparticle density increased, conduction effect could have slightly increased the conductance capacity of the wick with respect to the 9% vol/vol (66% wt./wt.). Overall, however, the enhancement after 1% is minimal. A percentage of 1% vol/vol agrees well with information in literature on Alumina nanofluids, and so seems to also apply to immobilized nanoparticles.

#### 4.7 Effect of Wick Thickness on the Integrated and Non-Integrated Wicks

Further tests were done with a more conductive nanopowder -- Cu nanoparticles, to gauge the power production enhancement, using the 1% vol/vol concentration. This test is done for different wick thicknesses: 0.024", 0.062", 0.125" and 0.250"; juxtaposed with their plain wick counterparts to observe the contribution of the immobilized nanoparticle to thermoelectric power generation as the wick thickness increased (Figs. 35 - 38).

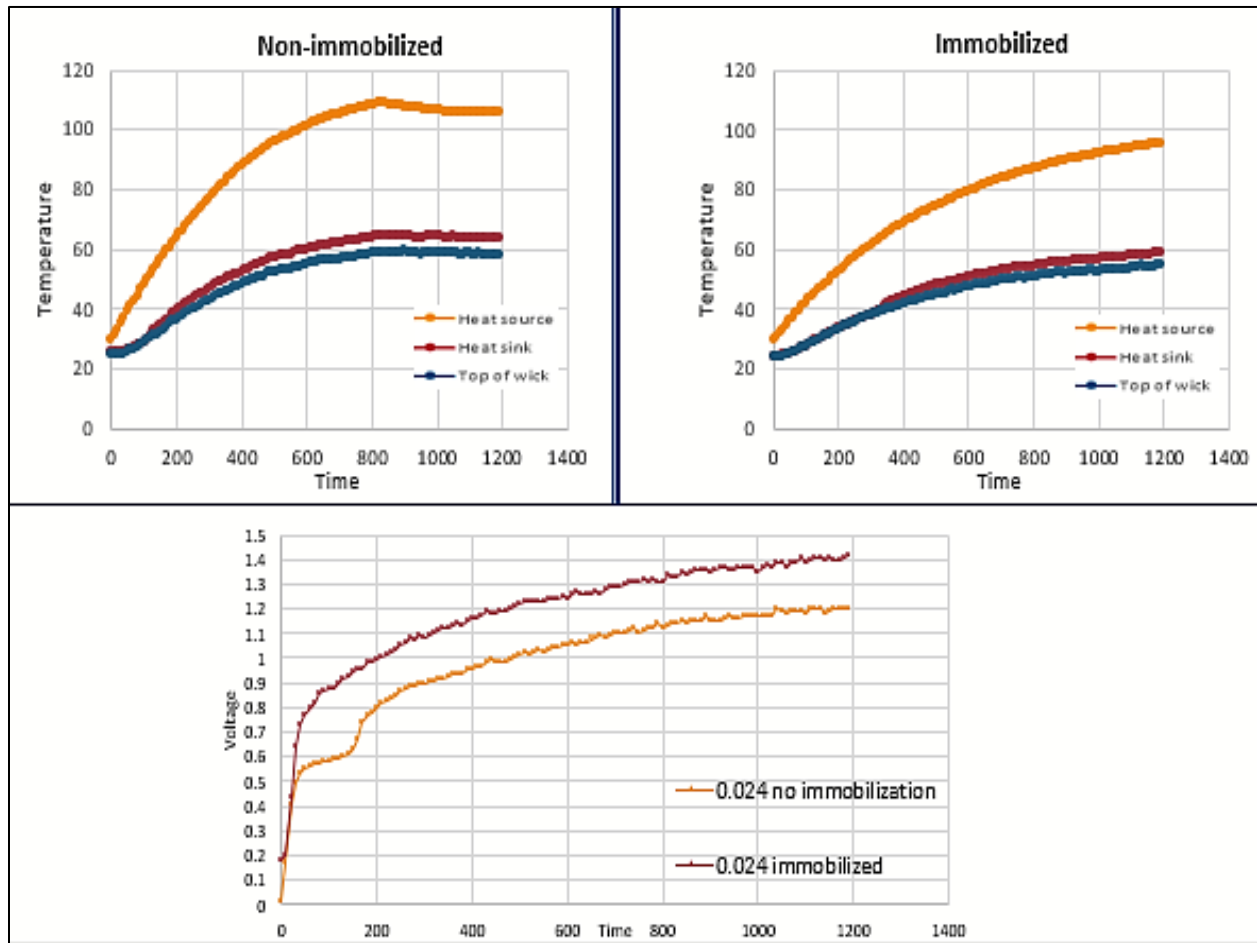


Figure 35: Temperature difference and voltage results for 0.024" wick

The integrated PE wick, being more conductive by virtue of the immobilized nanoparticles, reduced the temperature of the heat source compared to the plain PE wick, despite equal power input. This is attributed to its ability to pump away the thermal energy faster. Also, the disparity

in the temperature across the wick ( $\Delta T$  between heat sink and top of wick) for both integrated and plain PE wicks shows that the integrated PE wick has more conductance.

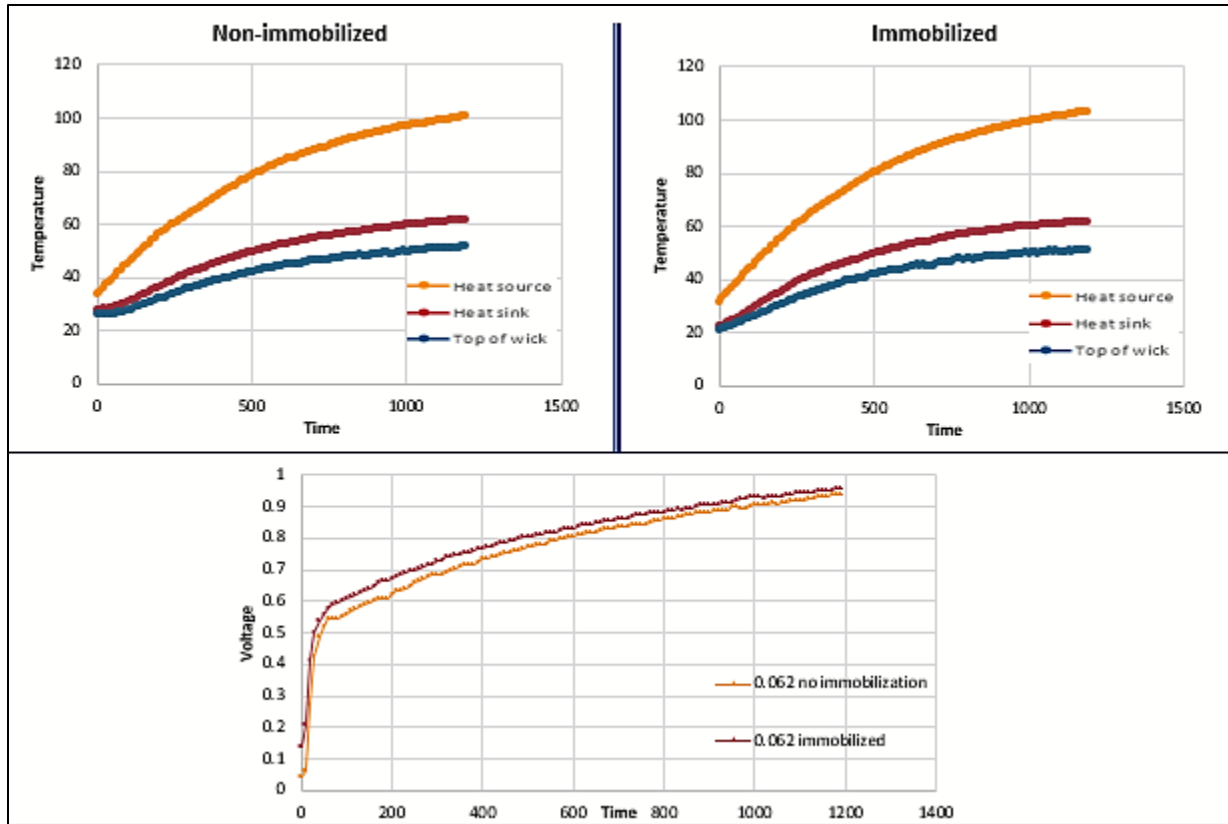


Figure 36: Temperature difference and voltage results for 0.062” wick

Fig. 36 suggests that as the wick thickness increases, the advantage that the immobilized nanoparticle offers the wick diminishes. The difference in conductance and voltage results after the 0.024” wick is negligible at best. Compared to Fig. 35, there is more disparity in the temperature across the 0.062” wick due to the greater radial distance for vapor transport. Figs. 37 and 38 show even more disparity in the temperature across their wicks compared to the preceding wick. For the 0.250” wick, the immobilization percentage has an adverse effect on its performance, probably due to its effect on the permeability; a much lower immobilization percentage may have a better result for the 0.025” wick if the hypothesis is correct. For 1% vol/vol nanoparticle suspension for immobilization, the 0.250” plain PE wick performs much better.

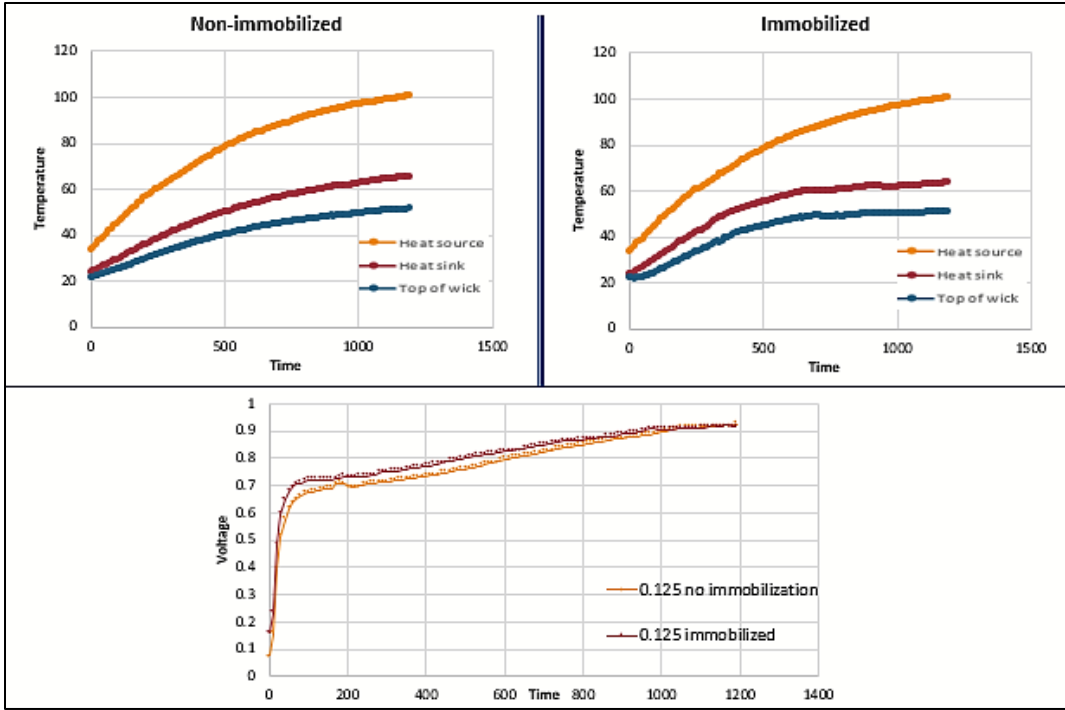


Figure 37: Temperature difference and voltage results for 0.125" wick

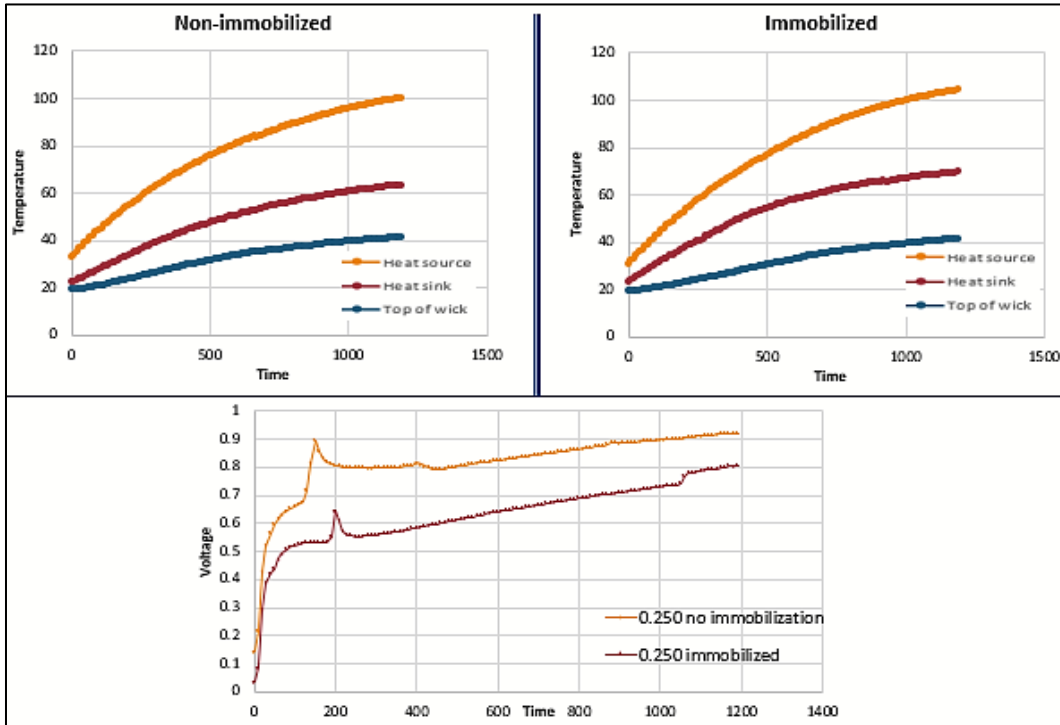


Figure 38: Temperature difference and voltage results for 0.250" wick

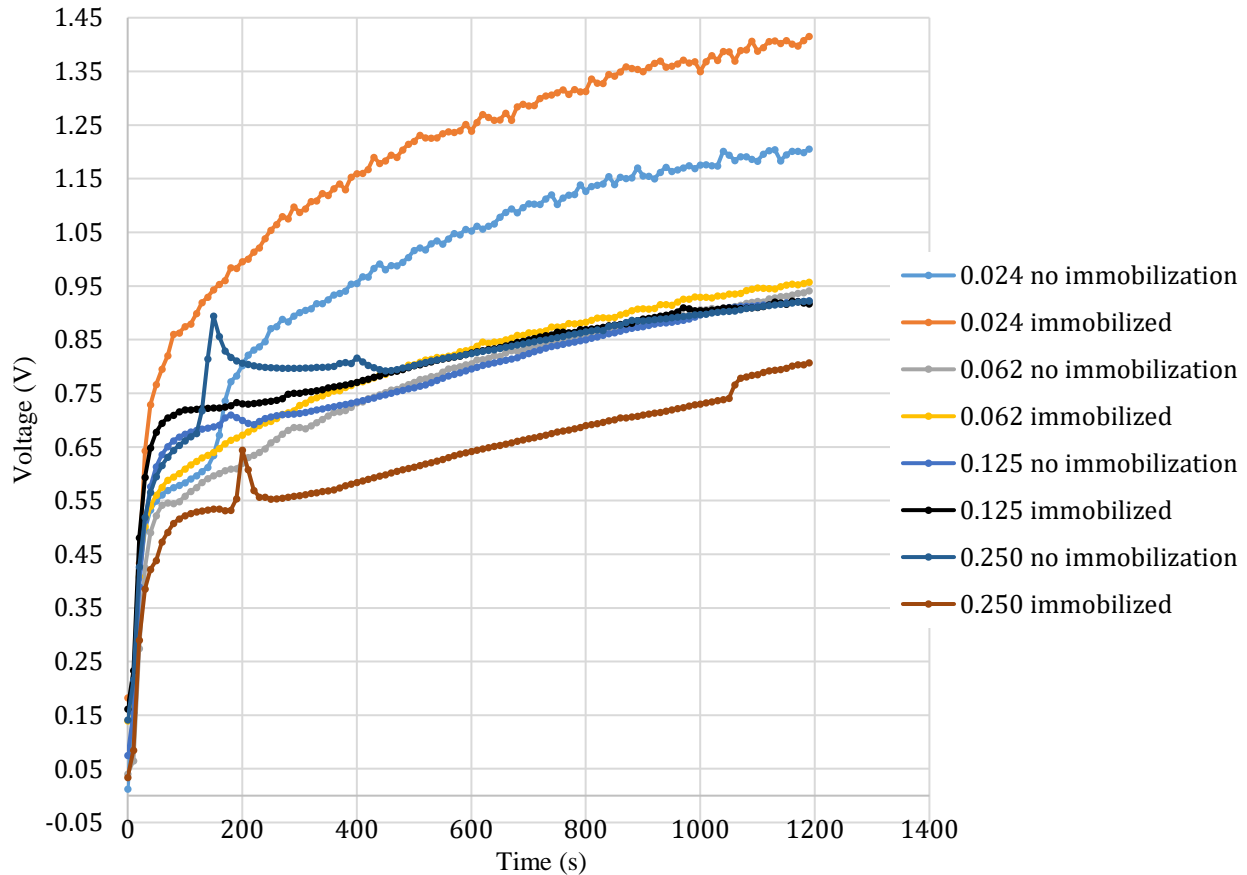


Figure 39: Summary of voltage results for all the wicks

From the foregoing, the wick with the most performance/lowest thermal resistance is the 0.024” (0.6mm) integrated PE wick. It was so effective at conducting away the heat that it reduced the temperature of the heat source more than the plain 0.024” wick, despite equal power input. Besides increased voltage potential, this also helps preserve the life of the TEGs, or other electronic device since this is of non-discriminatory utility.

An attempt to explain the decrease in voltage with increase in wick thickness follows thus: there are two ways the cooling is affected -- by conduction through the wick (conductance) and by latent heat contribution. The conductance decreases with thickness (per constant immobilized percentage) due to the increased distance for the vapor to travel.

Also, immobilization affects permeability and reduces porosity, according to observations. For the 0.024” wick this effect is not significant, and the conductance is much more effective due to the small travel length for thermal transport, unlike the 0.250” wick.

With increase in thickness, the conductance eventually gets dominated by the adverse effect of the hindrance of vapor transport. For the 0.250” integrated wick, the effect is complicated by the reduction in permeability so even less vapor can easily escape, which would contribute to more heat on the cold side, most probably in the form of superheated vapor, hence less temperature difference and less voltage obtained.

#### 4.8 Completed Heat Sink Test Run to Obtain 5V by Harvesting Low-Grade Heat

Two tests were carried out, one in a room with no recorded air velocity and the other subject to outdoor conditions (air velocity ranged from 1 m/s to 2m/s).

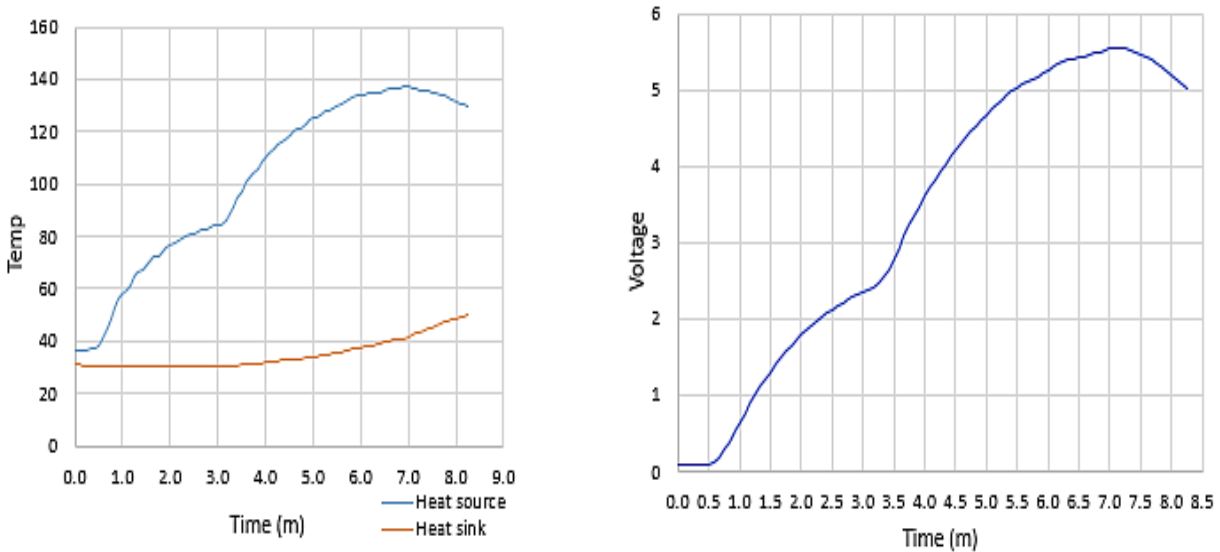


Figure 40: Temporal evolution of heat sink and source temperature, and the voltage for 0 m/s airflow.

This represents an extreme case with zero air movement, which would severely impede the convective current that the heat sink depends on to remain effective. 5V was attained with this

setup at  $\approx 94^{\circ}\text{C}$  temperature difference in about 5 minutes (there was no heat source for 30 seconds, at the beginning of the experiment).

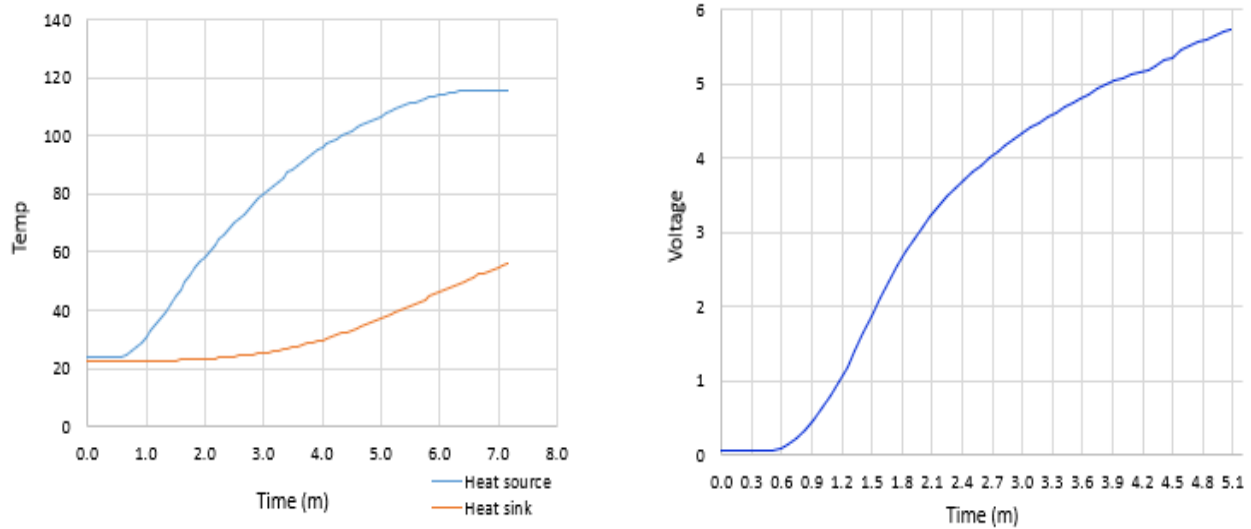
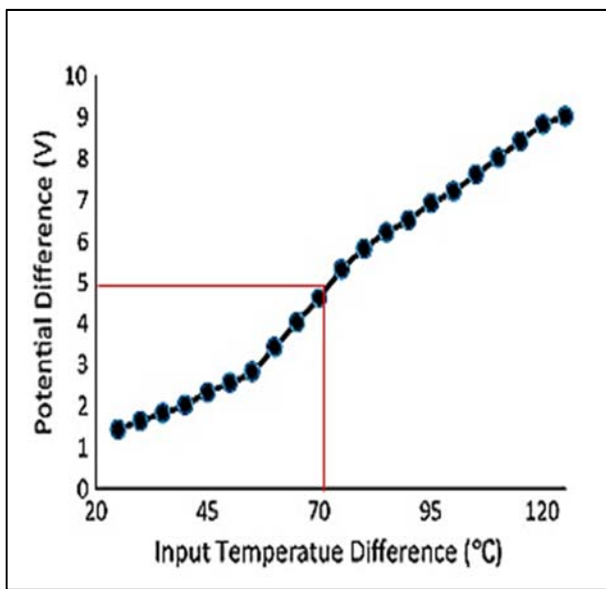


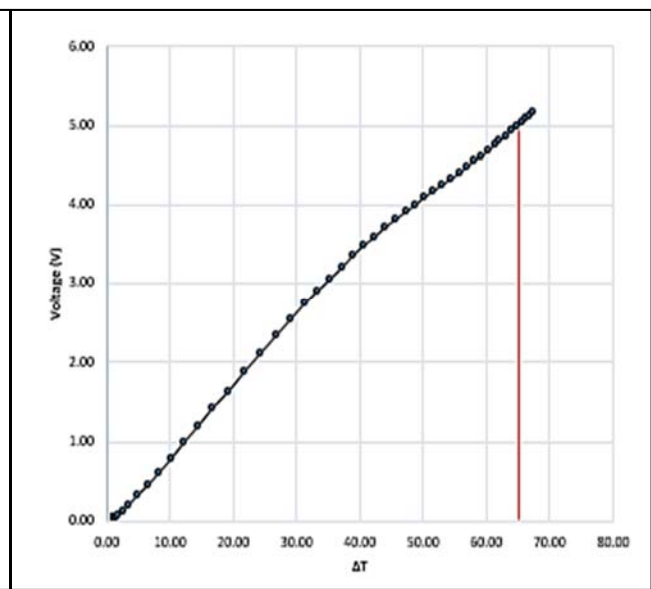
Figure 41: Temporal evolution of heat sink and source temperature, and the voltage for gentle airflow.

Here, with little air flow ( $< 2\text{m/s}$ ), which is representative of outdoor conditions, 5V was attained at about  $65^{\circ}\text{C}$  temperature difference in 3 minutes and 30 secs. This is consistent with predictions based on the Seebeck coefficient experiment/calculations before the experiment on using 8 TEGs for the device. The heat sink is able to dissipate the heat energy adequately aided by the novel curved base design and the PE wick with enhanced thermal management capability due to its integration with Cu nanoparticles.

Considering heat source is low grade heat and the heat sink utilizes a passive cooling process, attaining 5V with  $65^{\circ}\text{C}$  in 3.5 minutes is remarkable and underscores the efficacy of the heat sink design. For perspective, Fig. 42 is a comparison of this work and that of Mostafavi and Mahmoudi, 2018 [117]. In their work, 5V was attained at  $70^{\circ}\text{C}$  temperature difference with fan-assisted metal fin as heat sink. Here, 5V was attained at  $65^{\circ}\text{C}$  temperature difference with a passive, evaporatively-cooled heat sink using a PE wick integrated with Cu nanoparticles.



(a) Mostafavi and Mahmoudi, 2018



(b) Present work

Figure 42: The integrated PE wick heat sink outperformed an active heat sink from a recent study.

## CHAPTER 5. CONCLUSION AND RECOMMENDATIONS

A passive heat sink, designed as an evaporator-above-condenser system and capable of enabling 8 Bi<sub>2</sub>Te<sub>3</sub> TEGs attain enough thermal potential with low-grade waste heat so as to generate up to 5V, has been developed. A hydrophilic non-metal wick (polyethylene) integrated with Cu nanoparticles is used for the heat sink and its intrinsic low thermal conductivity prevented thermal leak to its compensation channels. This is the first time an integrated PE wick is investigated, and experimental evidence validates the hypothesis that the presence of immobilized nanoparticles improves the thermal management of the wick, so long as the radial distance in the y-direction is  $\lll$  x-direction. This enhancement, however, is not drastic. Results also show that the integrated non-metal wick delivers the same performance as a heat pipe without the attendant thermal leak to the reservoir/compensation chamber unlike loop heat pipes. The total production cost of the heat sink is less than \$20, and it is portable and eco-friendly.

The heat sink is able to deliver 5V in 3.5 minutes. This may not be instantaneous enough for consumers but there is the possibility of storing the energy in a power bank, to be used when needed. The voltage does not attain a steady state but fluctuates with respect to minute changes in temperature difference and heat source incident power. Due to the non-steady state of the voltage, the device may not be ideal for powering small electronic devices directly. To maintain a steady 5V, a voltage regulator/stabilizer may be used. The device can also be used with a voltage booster (step-up converter) to store auxiliary power for later use in homes and offices. Hours of harvesting low-grade waste heat passively from the ambient or any other source may store up enough energy for lighting and powering small devices.

Temperature difference in isolation is a misleading metric for judging thermoelectric voltage production potential. The thermal energy quality is crucial. Also, a good heat sink may attain a higher voltage with the same or even slightly less temperature difference as a less effective heat sink due to less external irreversibilities.

Thermal cycling effects on the system and small-scale energy storage via integration with a voltage regulator or booster is worth investigating further as this is a field with huge renewable energy

potential. Studies shows that 49.3–51.5% of global energy use would end up as waste heat by 2030 [1] and over 65% of that waste heat will be low-grade waste heat. Waste heat recovery is a fast growing billion-dollar energy market and this work clearly shows that passive, efficient harvesting of low-grade waste heat with TEGs is possible.

## REFERENCES

- [1] Firth A., Zhang B., Yang A., 2019, "Quantification of global waste heat and its environmental effects", *Applied Energy*, Vol. 235, pp. 1314-1334.
- [2] Qiu K, Hayden A.C.S., 2011, "Development of thermoelectric self-powered heating equipment", *J. Electron Mater*; 40:606–10.
- [3] Jeong E.S., 2014, "A new approach to optimize thermoelectric cooling modules", In *Cryogenics*, Volume 59, 2014, Pages 38-43.
- [4] Muhammad S., Ibrahim H., Aziz R., 2017, "An overview of cooling of thermoelectric devices", In *Renewable and Sustainable Energy Reviews*, Volume 78, 2017, Pages 15-22.
- [5] Pereira A, Caroff T, Lorin G, Baffie T, Romanjek K, Vesin S, Kusiaku K, Duchemin H, Salvador V, Miloud-Ali N, Aixala L, Simon J., 2015, "High temperature solar thermoelectric generator – indoor characterization method and modeling". *Energy*, 84: 485–92.
- [6] Amatya R, Ram R.J., 2010, "Solar thermoelectric generator for micropower applications. *J Electron Mater*, 39: 1735–40.
- [7] Chávez-Urbiola E.A, Vorobiev Y.V, Bulat L.P., 2012, "Solar hybrid systems with thermoelectric generators", *Sol Energy*, 86: 369–78.
- [8] Lertsatitthanakorn C., 2007, "Electrical performance analysis and economic evaluation of combined biomass cook stove thermoelectric (BITE) generator". *Bioresour Technol.*, 98: 1670–4.
- [9] Candadai A.A, Kumar V.P, Barshilia H.C., 2016, "Performance evaluation of a natural convective-cooled concentration solar thermoelectric generator coupled with a spectrally selective high temperature absorber coating". *Sol Energy Mater Sol Cells*, 145(Part 3):333–41.
- [10] Singh R., Tundee S., Akbarzadeh A., 2011, "Electric power generation from solar pond using combined thermosyphon and thermoelectric modules". *Sol Energy*, 85:371–8.
- [11] Champier D, Bédécarrats J.P, Kousksou T., Rivaletto M., Strub F., Pignolet P., 2011, "Study of a TE (thermoelectric) generator incorporated in a multifunction wood stove", *Energy*, 36: 1518–26.
- [12] Gou X, Xiao H, Yang S., 2010, "Modeling, experimental study and optimization on low temperature waste heat thermoelectric generator system", *Appl Energy*, 87:3131–6.
- [13] Hsu C.T, Yao D.J, Ye K.J, Yu B., 2010, "Renewable energy of waste heat recovery system for automobiles". *J Renew Sustain Energy*, 2:013105.

- [14] Hsu C.T, Huang G.Y, Chu H.S, Yu B., Yao D.J., 2011, “Experiments and simulations on low-temperature waste heat harvesting system by thermoelectric power generators”, *Appl Energy*, 88: 1291–7.
- [15] Mgbemene C.A, Duffy J., Sun H., Onyegebu S.O., 2010, “Electricity generation from a compound parabolic concentrator coupled to a thermoelectric module”, *J Sol Energy Eng.*, 132:031015.
- [16] Suter C., Tomeš P., Weidenkaff A., Steinfeld A., 2011, “A solar cavity-receiver packed with an array of thermoelectric converter modules”, *Sol Energy*, 85:1511–8.
- [17] Zhang M., Miao L., Kang Y.P., Tanemura S., Fisher C.A.J., Xu G., Li C.X., Fan G.Z., 2013, “Efficient, low-cost solar thermoelectric co-generators comprising evacuated tubular solar collectors and thermoelectric modules”, *Appl Energy*, 109: 51–9.
- [18] Chen W.H., Liao C.Y., Hung C.I., Huang W.L., 2012, “Experimental study on thermoelectric modules for power generation at various operating conditions”, *Energy* 45:874–81.
- [19] Fan H., Singh R., Akbarzadeh A., 2011, “Electric power generation from thermoelectric cells using a solar dish concentrator”, *J. Electron Mater*, 40:1311–20.
- [20] Kim S., Park S., Kim S., Rhi S.H., 2011, “A thermoelectric generator using engine coolant for light-duty internal combustion engine-powered vehicles”, *J Electron Mater*, 40:812–6.
- [21] Remeli M.F., Tan L., Date A., Singh B., Akbarzadeh A., 2015, “Simultaneous power generation and heat recovery using a heat pipe assisted thermoelectric generator system”, *Energy Convers Manage*, 91:110–9.
- [22] Elghool A., Basrawi F., Ibrahim T.K., Habib K., Ibrahim H., Idris D.M.N.D, 2017, “A review on heat sink for thermo-electric power generation: Classifications and parameters affecting performance”, In *Energy Conversion and Management*, Volume 134, pp 260-277.
- [23] Jaworski M., Bednarczyk M., Czachor M., 2016, “Experimental investigation of thermoelectric generator (TEG) with PCM module”, In *Applied Thermal Engineering*, Volume 96, pp 527-533.
- [24] Chen X., Ye H., Fan X., Ren T., Zhang G., 2016, “A review of small heat pipes for electronics”, In *Applied Thermal Engineering*, Volume 96, pp 1-17.
- [25] Li J., Wang D., Peterson G.P., 2010, “Experimental studies on a high-performance compact loop heat pipe with a square flat evaporator”, In *Applied Thermal Engineering*, Volume 30, Issues 6–7, pp 741-752.
- [26] Yakomaskin A.A., Afanasiev V.N., Zubkov N.N., Morskoy D.N., 2013, “Investigation of Heat Transfer in Evaporator of Microchannel Loop Heat Pipe”. *ASME. J. Heat Transfer*, 135(10):101006-101006-7.

- [27] Nagano, H., Ogawa, H., Fukuyoshi, F., and Nagai, H., 2009, "Fabrication and Testing of a Small Loop Heat Pipe With a Plastic Wick," International Conference on Heat Pipes for Space Application, Moscow.
- [28] Boo, J. H., and Chung, W. B., 2005, "Experimental Study on the Thermal Performance of a Small-Scale Loop Heat Pipe With Polypropylene Wick," *J. Mech. Sci. Technol. (KSME Int. J.)*, 19(4), pp. 1052–1061.
- [29] Dolgirev, Y. E., Maydanik, Y. F., and Fershtater, Y. G., 1983, "Influence of Thermal Conductivity of a Wick on Temperature of an Antigravitational Heat Pipe," *Phase Changes in Metastable Systems, Sverdlovsk, USC AS USSR*, pp. 23–27.
- [30] Nnanna A.G., Rutherford W., Elomar W., Sankowski B., 2009, "Assessment of thermoelectric module with nanofluid heat exchanger", *Applied Thermal Engineering*, Volume 29, Issues 2–3, Pages 491-500.
- [31] Nnanna A. G. 2007, "Experimental model of temperature-driven nanofluid", *Journal of Heat Transfer*. June issue.
- [32] Xuan, Y., and Roetzel, W., 2000, "Conceptions for Heat Transfer Correlation of Nanofluids," *Int. J. Heat Mass Transfer*, 43, pp. 3701–3707.
- [33] Lee, S., and Choi, S. U. S., 1996, "Application of Metallic Nanoparticle Suspensions in Advanced Cooling Systems," *"ASME Recent Advances in Solids/Structures and Application of Metallic materials"*, PVP (Am. Soc. Mech. Eng.)-Vol. 342 /MD-Vol. 72, pp. 227–234.
- [34] Shirakawa H., Louis E.J., MacDiarmid A.G., Chiang C.K., Heeger A.J., 1977, *J. Chem. Soc. Chem. Commun.* 0, p.578.
- [35] Bozell J.J., Petersen G.R., 2010, *Green Chem.* 12, p.539.
- [36] van Putten R.-J., van der Waal J.C., de Jong E., Rasrendra C.B., Heeres H.J., de Vries J.G., 2013, *Chem. Rev.* 113, pp.1499–1597.
- [37] Beretta D., Neophytou N., Hodges J. M., Kanatzidis M. G., Narducci D., Martin- Gonzalez M., Beekman M., Balke B., Cerretti G., Tremel W., Zevalkink A, Hofmann A. I., Müller C., Dörling B., Campoy-Quiles M., Caironi M., 2018, "Thermoelectrics: From history, a window to the future", *Materials Science and Engineering: R: Reports*.
- [38] Dipak S. P., Rachayya R. A., Pramod V. W., 2018, "Thermoelectric materials and heat exchangers for power generation – A review", *Renewable and Sustainable Energy Reviews*, Volume 95, pp. 1-22.
- [39] Goldsmid H.J. and Douglas R.W., 1954, *Br. J. Appl. Phys.* 5, p.386.
- [40] DiSalvo F.J., 1999, *Science* 285, pp.703–706.

- [41] Goldsmid H.J., 2016, *Introduction to Thermoelectricity*, Springer, Berlin Heidelberg, Berlin, Heidelberg.
- [42] LaLonde A.D., Pei Y., Wang H., Jeffrey G.S., 2011, *Mater. Today* 14 pp.526–532.
- [43] Wood C., 1988, *Rep. Prog. Phys.* 51, pp.459–539.
- [44] REGULATION (EC) No 443/2009 OF THE EUROPEAN PARLIAMENT AND OF THE COUNCIL, 2009, "Setting Emission Performance Standards for New Passenger Cars As Part of the Community's Integrated Approach to Reduce CO<sub>2</sub> Emissions From Light-duty Vehicles".
- [45] Lee S., Esfarjani K., Luo T., Zhou J., Tian Z., Chen G., 2014, *Nat. Commun.* 5, p.3525.
- [46] Sootsman J.R., Chung D.Y., Kanatzidis M.G., 2009, *Angew. Chemie Int. Ed.* 48, pp.8616–8639.
- [47] Nielsen M.D., Ozolins V., Heremans J.P., 2013, *Energy Environ. Sci.* 6, pp.570–578.
- [48] Zhao L.-D., Chang C., Tan G., Kanatzidis M.G., 2016, *Energy Environ. Sci.* 9 pp.3044–3060.
- [49] Han C., Sun Q., Li Z., Dou S.X., 2016, *Adv. Energy Mater.* 6, 1600498.
- [50] Tan G., Zhao L.-D., Kanatzidis M.G., 2016, *Chem. Rev.* 116, pp.12123–12149.
- [51] Elsheikh MH et al., 2014, "A review on thermoelectric renewable energy: principle parameters that affect their performance". *Renew Sustain Energy Rev*; 30:337–55.
- [52] Satterthwaite, C. B.; Ure, R., 1957, "Electrical and Thermal Properties of Bi<sub>2</sub>Te<sub>3</sub>". *Phys. Rev.* 108 (5): 1164.
- [53] LeBlanc S., 2014, "Thermoelectric generators: linking material properties and systems engineering for waste heat recovery applications", *Sustain Mater Technol*;1–2:26–35.
- [54] Tzeng S.C., Jeng T.M., Lin Y.L., 2014, "Parametric study of heat-transfer design on the thermoelectric generator system", *Int. Commun Heat Mass Transf*; 52:97–105.
- [55] Xiaozong C., Leifeng L., Yuan D., Lianjun W., Lidong C., Wan J., 2012, "Preparation of nano-sized Bi<sub>2</sub>Te<sub>3</sub> thermoelectric material powders by cryogenic grinding", *Prog Nat Sci: Mater Int*; 22(3):201–6.
- [56] Rowe, D.M. (2005), *Thermoelectrics Handbook: Macro to Nano*, CRC Press, ISBN 978-1-4200-3890-3.
- [57] Paothep P., Prabhakar B., 2010, "Nanostructured thermoelectrics", *Mater Sci Eng; R* 67:19–63.

- [58] Rowe D.M., 1994, "Thermoelectric generators as alternative sources of low power", *Renew Energ*; 5(Part IL): 1470–8.
- [59] Rowe D.M., 1991, "Applications of nuclear-powered thermoelectric generators in space", *Appl Energy*; 40(241):271.
- [60] Hamid M.E., Abdulameer S.D., MohdFaizul M., Binti M.S., Haji H.M., Bashir A.M., Mahazani M., 2014, "A review on thermoelectric renewable energy: principle parameters that affect their performance". *Renew Sustain Energy Rev*; 30:337–55.
- [61] Wei H., Gan Z., Xingxing Z., Jie J., Guiqiang L., Xudong Z., 2015, "Recent development and application of thermoelectric generator and cooler", *Appl Energy*; 143:1–25.
- [62] Sevan K., Altug S., Fatih O.Z., Sahin T. S., 2012, "Characterization of a thermoelectric generator at low temperatures", *Energy Convers Manag*; 62:47–50.
- [63] Hilaal A., Seeram R., 2013, "A review on the enhancement of figure of merit from bulk to nano-thermoelectric materials". *Nano Energy*; 2:190–212.
- [64] Gonc-alves A.P, Lopes E.B, Delaizir G., Vaney J.B., Lenoir B., Piarristeguy A., Pradel A., Monnier J., Ochin P., Godart C., 2012, "Semiconducting glasses: a new class of thermoelectric materials". *J Solid State Chem*; 193:26–30.
- [65] Delaire O., May A.F., McGuire M.A., Porter W.D., Lucas M.S., Stone M.B., Abernathy D.L., Ravi V.A., Firdosy S.A., Snyder G.J., 2009, *Phys. Rev. B* 80, 184302.
- [66] May A.F., Singh D.J., Snyder G.J., 2009, *Phys. Rev. B* 79, 153101.
- [67] Zhao L.-D., Lo S.-H., Zhang Y., Sun H., Tan G., Uher C., Wolverton C., Dravid V.P., Kanatzidis M.G., 2014, *Nature* 508, pp.373–377.
- [68] Xu X., Dessel S.V. and Messacb A., 2007, "Study of the Performance of Thermoelectric Modules for Use in Active Building Envelopes," *Building and Environment*, Vol. 42, No. 3, pp. 1489-1502. <http://dx.doi.org/10.1016/j.buildenv.2005.12.021>.
- [69] Lin H., Tan G., Shen J.-N., Hao S., Wu L.-M., Calta N., Malliakas C., Wang S., Uher C., Wolverton C., Kanatzidis M.G., 2016, *Angew. Chemie Int. Ed.* 55, pp.11431–11436.
- [70] Tan G., Hao S., Zhao J., Wolverton C., Kanatzidis M.G., 2017, *J. Am. Chem. Soc.* 139, pp.6467–6473.
- [71] Pei Y., Chang C., Wang Z., Yin M., Wu M., Tan G., Wu H., Chen Y., Zheng L., Gong S., Zhu T., Zhao X., Huang L., He J., Kanatzidis M.G., Zhao L.-D., 2016, *J. Am. Chem. Soc.* 138, pp.16364–16371.

- [72] Montecucco A., Knox A. R., 2014, "Accurate simulation of thermoelectric power generating systems", *Appl Energy*; 118:166–72.
- [73] Brazier K., <https://commons.wikimedia.org>
- [74] Khattab N.M., Shenawy E.T., 2006, "Optimal operation of thermoelectric cooler driven by solar thermoelectric generator", *Energy Convers Manag*; 47:407–26.
- [75] Özkaynak S., Göktun S., 1994, "Effect of irreversibilities on the performance of a thermoelectric generator", *Energy Conversion and Management*; 35 (issue 12): pp 1117-1121.
- [76] Yue R., Xu J., 2012, "Poly(3,4-ethylenedioxythiophene) as promising organic thermoelectric materials: a mini-review", *Synth Met*; 162:912–7.
- [77] Rowe D.M., 1999, "Thermoelectrics, an environmentally-friendly source of electrical power", *Renew Energy*; 16:1251–6.
- [78] Riffat S.B., Xiaoli M., 2003, "Thermoelectrics: a review of present and potential applications", *Appl Therm Eng*; 23:913–35.
- [79] Champier D., Bedecarrats J.P., Rivaletto M., Strub F., 2010, "Thermoelectric power generation from biomass cook stoves", *Energy*; 35:935–42.
- [80] Champier D., Bédécarrats J.P., Kousksou T., Rivaletto M., Strub F., Pignolet P., 2011, "Study of a TE (thermoelectric) generator incorporated in a multifunction wood stove", *Energy*; 36:1518–26.
- [81] Risha M., Rajendra P., Virendra V.K, Amit V.R., 2015, "The design, development and performance evaluation of thermoelectric generator (TEG) integrated forced draft biomass cookstove", *Procedia Comput Sci*; 52:723–9.
- [82] Wei H., Gan Z., Xingxing Z., Jie J., Guiqiang L., Xudong Z., 2015, "Recent development and application of thermoelectric generator and cooler", *Appl Energy*; 143:1–25.
- [83] Rowe D.M., 1981, "A high performance solar powered thermoelectric generator *Appl Energy*, 8, pp. 269-273.
- [84] Tomeš P., Trottmann M., Suter C., Aguirre M.H., Steinfeld A., Haueter P., Weidenkaff A., 2010, "Thermoelectric oxide modules (TOMs) for the direct conversion of simulated solar radiation into electrical energy", *Materials*, 3, pp. 2801-2814.
- [85] Weidenkaff A., Trottmann M., Tomeš P., Suter C., Steinfeld A., Veziridis A., 2013, "Solar TE converter applications", *Thermoelectric nanomaterials*, 182, Springer Berlin Heidelberg, pp. 365-382.

- [86] Nguyen N.Q., Pochiraju K.V., 2013, "Behavior of thermoelectric generators exposed to transient heat sources", *Appl Therm Eng*, 51, pp. 1-9.
- [87] Wang C.-C., Hung C.-I., Chen W.-H., 2012, "Design of heat sink for improving the performance of thermoelectric generator using two-stage optimization" *Energy*, 39, pp. 236-245.
- [88] Gou X., Xiao H., Yang S., 2010, "Modeling, experimental study and optimization on low-temperature waste heat thermoelectric generator system" *Appl Energy*, 87, pp. 3131-3136.
- [89] Crane D.T., Jackson G.S., 2004, "Optimization of cross flow heat exchangers for thermoelectric waste heat recovery" *Energy Convers Manag*, 45, pp. 1565-1582.
- [90] Mastbergen D., Willson B., 2005, "Generating light from stoves using a thermoelectric generator". In: *Proceedings of the ETHOS international stove research conference*.
- [91] Su C.Q., Xu M., Wang W.S., Deng Y.D., Liu X., Tang Z.B., 2015, "Optimization of cooling unit design for automotive exhaust-based thermoelectric generators", *J Electron Mater*, 44, pp. 1876-1883.
- [92] Ma Z., Wang X., Yang A., 2014, "Influence of temperature on characters of thermoelectric generators based on test bed" *J Nanomater*, p. 6.
- [93] Kim S., Park S., Kim S., Rhi S.-H., 2011, "A thermoelectric generator using engine coolant for light-duty internal combustion engine-powered vehicles" *J Electron Mater*, 40, pp. 812-816.
- [94] Hsu C.-T., Yao D.-J., Ye K.-J., Yu B., 2010, "Renewable energy of waste heat recovery system for automobiles", *J Renew Sustain Energy*, 2, p. 013105.
- [95] Huang G.-Y., Hsu C.-T., Fang C.-J., Yao D.-J., 2016, "Optimization of a waste heat recovery system with thermoelectric generators by three-dimensional thermal resistance analysis", *Energy Convers Manag*, 126, pp. 581-594.
- [96] Hsu C.-T., Huang G.-Y., Chu H.-S., Yu B., Yao D.-J., 2011, "Experiments and simulations on low-temperature waste heat harvesting system by thermoelectric power generators", *Appl Energy*, 88, pp. 1291-1297.
- [97] Niu X., Yu J., Wang S., 2009, "Experimental study on low-temperature waste heat thermoelectric generator", *J Power Sources*, 188, pp. 621-626.

- [98] Chen W.-H., Liao C.-Y., Hung C.-I., Huang W.-L., 2012, "Experimental study on thermoelectric modules for power generation at various operating conditions" *Energy*, 45, pp. 874-881.
- [99] Zhang M., Miao L., Kang Y.P., Tanemura S., Fisher C.A.J., Xu G., Li C.X., Fan G.Z., 2013, "Efficient, low-cost solar thermoelectric cogenerators comprising evacuated tubular solar collectors and thermoelectric modules", *Appl Energy*, 109, pp. 51-59.
- [100] Olsen M.L., Warren E.L., Parilla P.A., Toberer E.S., Kennedy C.E., Snyder G.J., Firdosy S.A., Nesmith B., Zakutayev A., Goodrich A., Turchi C.S., Netter J., Gray M.H., Ndione P.F., Tirawat R., Baranowski L.L., Gray A., Ginley D.S., 2014, "A high-temperature, high-efficiency solar thermoelectric generator prototype" *Energy Procedia*, 49, pp. 1460-1469.
- [101] Muthu G., Shanmugam S., Veerappan A.R., 2014, "Solar parabolic dish thermoelectric generator with acrylic cover", *Energy Procedia*, 54, pp. 2-10.
- [102] Eswaramoorthy M., Shanmugam S., Veerappan A., 2013, "Experimental study on solar parabolic dish thermoelectric generator", *Int J Energy Eng*, 3, p. 62.
- [103] Yazawa K., Wong V.K., Shakouri A., 2012, "Thermal challenges on solar concentrated thermoelectric CHP systems", In: *Proceedings of the 2012 13th IEEE intersociety conference on thermal and thermomechanical phenomena in electronic systems (ITherm)*; p. 1144–50.
- [104] Fan H., Singh R., Akbarzadeh A., 2011, "Electric power generation from thermoelectric cells using a solar dish concentrator", *J Electron Mater*, 40, pp. 1311-1320.
- [105] Aranguren P., Astrain D., Pérez M.G., 2014, Computational and experimental study of a complete heat dissipation system using water as heat carrier placed on a thermoelectric generator *Energy*, 74, pp. 346-358.
- [106] Aranguren P., Astrain D., Martínez A., 2014, "Study of complete thermoelectric generator behavior including water-to-ambient heat dissipation on the cold side", *J Electron Mater*, 43, pp. 2320-2330.
- [107] Champier D., Bédécarrats J.P., Kousksou T., Rivaletto M., Strub F., Pignolet P., 2011, "Study of a TE (thermoelectric) generator incorporated in a multifunction wood stove" *Energy*, 36, pp. 1518-1526.

- [108] Ozeh M., Nnanna A., 2018, "Waste Heat Recovery for Powering Mobile Devices Using Thermoelectric Generators and Evaporatively-Cooled Heat Sink", ASME, International Electronic Packaging Technical Conference and Exhibition, ASME 2018 International Technical Conference and Exhibition on Packaging and Integration of Electronic and Photonic Microsystems, doi:10.1115/IPACK2018-8354.
- [109] Date A., Date A., Dixon C., Singh R., Akbarzadeh A., 2015, "Theoretical and experimental estimation of limiting input heat flux for thermoelectric power generators with passive cooling", *Sol Energy*, 111, pp. 201-217.
- [110] Nuwayhid R.Y., Hamade R., 2005, "Design and testing of a locally made loop-type thermosyphonic heat sink for stove-top thermoelectric generators", *Renew Energy*, 30, pp. 1101-1116.
- [111] Djafar Z., Putra N., Koestoer R.A., 2013, "The utilization of heat pipe on cold surface of thermoelectric with low-temperature waste heat", *Appl Mech Mater*, pp. 410-415.
- [112] He W., Su Y., Wang Y.Q., Riffat S.B., Ji J., 2012, "A study on incorporation of thermoelectric modules with evacuated-tube heat-pipe solar collectors", *Renew Energy*, 37, pp. 142-149.
- [113] He W., Su Y., Riffat S.B., Hou J., Ji J., 2011, "Parametrical analysis of the design and performance of a solar heat pipe thermoelectric generator unit", *Appl Energy*, 88, pp. 5083-5089.
- [114] makeitfrom.com. (2018). 3003-H14-Aluminum. [online] Available at: <https://www.makeitfrom.com/material-properties/3003-H14-Aluminum> [Accessed 24 Jun. 2019].
- [115] De Kerpel K., De Schamphelleire S., Steuperaert H., De Jaeger P., De Paepe M., 2016, "Experimental study of the effect of felt wick porosity on capillary-driven heat pipes", *Applied Thermal Engineering*, Vol. 96, pp. 690-698.
- [116] Incropera F. P., Dewitt D. P., Bergman T. L., Lavine A. S., 2007, "Introduction to Heat Transfer", 5<sup>th</sup> Ed., John Wiley and Sons, United States, p 779.
- [117] Mostafavi S. A., Mahmoudi M., 2018, "Modeling and fabricating a prototype of a thermoelectric generator system of heat energy recovery from hot exhaust gases and evaluating the effects of important system parameters", *Applied Thermal Engineering*, Vol. 132, pp. 624-636.